Sedimentary Geology 342 (2016) 218–236

Contents lists available at ScienceDirect

Sedimentary Geology

journal homepage: www.elsevier.com/locate/sedgeo

Sedimentology, petrography and early diagenesis of a travertine–colluvium succession from Chusang (southern Tibet)

Zhijun Wang [a], Michael C. Meyer [a,*], Dirk L. Hoffmann [b]

[a] Institute of Geology, University of Innsbruck, Innrain 52, 6020 Innsbruck, Austria
[b] Department of Human Evolution, Max Planck Institute for Evolutionary Anthropology, D-04103 Leipzig, Germany

ARTICLE INFO

Article history:
Received 15 March 2016
Received in revised form 30 June 2016
Accepted 3 July 2016
Available online 12 July 2016

Editor: Dr. B. Jones

Keywords:
Tibetan Plateau
Hydrothermal spring carbonate
Travertine
Colluvium
Early diagenesis
Monsoon

ABSTRACT

The Chusang travertine is situated in southern Tibet at an altitude of ~4200 m asl. in a cold-arid, periglacial environment and is characterized by interbedding of hydrothermal carbonate with colluvium. Here we present sedimentological and petrographical data to elucidate the depositional environment and sedimentary processes responsible for hydrothermal carbonate precipitation and early diagenetic alteration as well as clastic sediment accumulation and provide initial ^{230}Th/U ages to constrain the time-depth of this travertine–colluvium succession. Three main travertine lithofacies have been identified: 1) a dense laminated lithofacies, 2) a porous layered lithofacies and 3) an intraclastic lithofacies that results from erosion of pre-existing hot spring carbonate. The colluvium is composed of cohesive debris flow layers that derived from mass-wasting events from the adjacent hillslopes. Micro-fabric analyses suggest that dense laminated travertine forms via rapid calcite precipitation from hot spring water seasonally subjected to severe winter cooling, while porous layered travertine results from seasonal dilution of hot spring water with rain water during the summer monsoon months, which in turn stimulates biological productivity and gives rise to a porous summer layer. Early diagenesis in the form of recrystallization and extensive formation of pore cements is common in the Chusang travertine, but never eradicates the original crystal fabrics completely.

The sedimentary architecture of the deposit is conditioned by (i) the gently dipping (~10°) pre-existing terrain on which hot spring water is discharged from multiple travertine mounds causing laterally extensive travertine sheets to precipitate, and (ii) the adjacent much steeper (up to 30°) periglacial hillslopes that are the source area of repeated debris flows that accumulate on the travertine surface. The resulting travertine–colluvium succession has a total thickness of ~24 m and ^{230}Th/U dating suggests that the base of this succession has a minimum age of ~486 ka, while the upper part (top-most ~8 m) of the succession started accumulating in the earliest Holocene. We hypothesize that hot spring activity (and thus travertine precipitation) and the occurrence of debris flow events has a climatic nexus, i.e. are both triggered by phases of enhanced Indian summer monsoon.

1. Introduction

Travertines are continental spring carbonates that precipitate from hydrothermal water (generally >30 °C in temperature) and that are typically bound to crustal-scale faults in extensional tectonic regimes (Özkul et al., 2002; Zentmyer et al., 2008; Capezzuoli et al., 2014; Della Porta, 2015; Croci et al., 2016). High rates of carbonate precipitation are common in travertines (frequently ≥1 cm/year; Pentecost, 2005) with two major consequences: (i) rapid crystal growth that results in high primary porosity, and (ii) high temporal resolution of proxy signals stored in these deposits. The latter effect is often expressed as lamination that resolves climate and temperature variability on a seasonal (Chafetz and Folk, 1984; Liu et al., 2010), and sometimes monthly or even diurnal scale (Chafetz and Folk, 1984; Takashima and Kano, 2008). Furthermore, spring carbonates such as travertines are – at least in principle – amenable to uranium-series disequilibrium dating (e.g. ^{230}Th/U dating; Mallick and Frank, 2002; Garnett et al., 2004; Stone et al., 2010) as well as luminescence dating (Rich et al., 2003; Mahan et al., 2007; Vazquez-Urbez et al., 2011), and are hence valuable archives of paleoclimatic and paleoenvironmental change (Frank et al., 2000; Minissale et al., 2002; Faccenna et al., 2008; Liu et al., 2010; Toker et al., 2015). In several reported instances travertines as well as other types of continental spring carbonates are also stratigraphically and/or spatially associated with archeological remains, especially in arid and semi-arid areas (the Tibetan highlands included) and can thus act as valuable archeological repositories too (Grün et al., 1988; Hill, 2001; Zhang and Li, 2002; Smith et al., 2004, 2007; Ashley et al., 2010).

Exploiting the paleoenvironmental and geoarcheological information stored in travertines is, however, impeded by the fact that these deposits are prone to early diagenesis, because of their high initial porosity

* Corresponding author.
E-mail address: michael.meyer@uibk.ac.at (M.C. Meyer).

http://dx.doi.org/10.1016/j.sedgeo.2016.07.002
0037-0738/

and permeability (Pentecost, 2005; Jones and Renaut, 2010; Capezzuoli et al., 2014). Diagenesis can alter the geochemical composition and thus paleoclimatic proxy signals recorded in spring carbonate deposits (Andrews, 2006), and also cause problems for ^{230}Th/U dating (e.g. open-system behavior with respect to uranium and/or thorium; Garnett et al., 2004; Stone et al., 2010). Moreover, detrital material (e.g. clay minerals) might afflict the quality of ^{230}Th/U dates of these deposits. Hence, a detailed study of the macroscopic and microscopic crystal fabrics and reconstruction of the depositional environments is necessary to gain insights into the sedimentary and diagenetic history of travertines (Chafetz and Folk, 1984; Jones and Renaut, 2008; Rainey and Jones, 2009) and to assess their fidelity as a paleoenvironmental archive.

On the Tibetan Plateau, hydrothermal springs and travertine deposits are common and preferentially occur along north–south trending active graben systems (Tong et al., 2000). Yet, in a Tibetan context, these hydrothermal spring carbonates are severely underresearched. Little is known about the nature of paleoclimatic information stored in these carbonates and the paleoenvironmental significance of past periods of travertine formation. The few Tibetan travertine sites that have been described so far include the Targjia and the Zabuye travertine (both central Tibet; Zhao et al., 2006; Zhao et al., 2010), the Nyalam travertine (southern Tibet; Zentmyer et al., 2008) and the Rongma travertine (northern Tibet; Gao et al., 2013). One particularly interesting travertine site is situated ca. 80 km northwest of Lhasa (Chusang; Fig. 1), where nineteen human hand- and footprints were discovered on the surface of the Chusang travertine (Zhang and Li, 2002), and are thought to be of Late Pleistocene age (Zhang and Li, 2002; Zhang et al., 2003), rendering Chusang an archeological key site for the Tibetan Plateau. Furthermore, the travertine deposit at Chusang is interbedded with colluvium and alluvium resulting in a ~24 m thick succession of hydrothermal carbonate and detrital terrigenous strata. Only very few examples of such mixed travertine-terrigenous successions have been described so far (e.g. Schulte et al., 2008; Zentmyer et al., 2008; Özkul et al., 2014; Claes et al., 2015; Croci et al., 2016), but these studies already highlight the variety of lithofacies types and different depositional architectures encountered in these deposits.

Alluvial fans and colluvial deposits are common on the Tibetan Plateau, owing to the sparse vegetation cover and periglacial processes operating on the hillslopes. Nevertheless, these unconsolidated sediments are also highly erodible; hence most of these terrigenous deposits reflect the latest Pleistocene and Holocene sedimentary dynamics on the plateau only (Wang and French, 1995; Kaiser et al., 2007, 2009). In the case of Chusang, however, the travertine layers are shielding the interbedded colluvial strata from erosion, and it is thus likely that in the stratigraphically lower part of the succession much older colluvium is preserved as compared to the adjacent hillslopes, allowing sediment based climate records to be extended back in time.

In this study, we conducted sedimentological and petrographic analyses on the travertine–colluvium succession of Chusang in order to reconstruct its stratigraphic architecture and depositional environment, to elucidate the processes responsible for travertine precipitation and to investigate the degree of diagenetic alteration. This work thus (i) lays the foundation for a ^{230}Th/U dating study, designed to provide an accurate chronological framework for the Chusang travertine succession and the human imprints encased in this carbonate (ii) is one of the first studies that focuses on the interplay between thermogene travertine and alluvial/colluvial deposition in a cold-arid periglacial environment and (iii) provides a conceptual model for the relationship between an enhanced summer monsoon and the sedimentary evolution of the Chusang succession.

2. Geomorphological setting and basic sedimentary architecture

The Chusang travertine is located near the village of Chusang (variously referred to as Quesang or Qiusang in the literature) about 80 km northwest of the city of Lhasa (Fig. 1). Today, the mean annual air temperature (MAAT) in the study area is ~4 °C (derived by adjusting the MAAT of Lhasa to an altitude of 4200 m asl. using the average atmospheric lapse rate of 0.65 °C/100 m) and the mean annual precipitation (MAP) is ~430 mm (data from the Public Weather Service Center of China). This part of the Tibetan Plateau is under the influence of the Indian and South Asian summer monsoon, delivering ca. 88% of the MAP between June and September (Public Weather Service Center of China).

The travertine deposit covers ~0.6 km^2 of a gently inclined (~5–12°) NW-facing slope between ~4070 m and 4280 m above sea level (asl.). Two hot springs with a discharge of ~0.1–0.3 L/s are present at the travertine site (Fig. 1). The main spring is situated at 4270 m asl. and is used in a public bath house (Fig. 1). Steeper slopes are surrounding the travertine and extend up to 4905 m asl. Periglacial slope and mass-wasting processes (frost creep, solifluction) and scarps formed by soil creep and active layer-detachment slides are abundant in the steeper upslope areas above ~4280 m (Fig. 1C, D). A ~560 m-long head scarp is present at the eastern end of the Chusang travertine at an elevation of 4300 m and ~185 m upslope of the main hot spring (Fig. 1C, D). Approximately 1.5 m of displacement and several fresh sinkholes can be observed along this scarp suggesting ongoing subrosion. No additional or superordinate landslides were observed in remote imagery or during the field campaigns at Chusang or in any of the adjacent catchments.

Two ephemeral streams incise into the Chusang travertine along its southern and northern margin, respectively (Fig. 1), exposing individual travertine sheets that alternate with layers of colluvial and occasionally alluvial sediment (Figs. 2, 3). Logging along the southern and the northern gully as well as inspection of outcrops along the street reveals at least seven such clastic layers (Fig. 4). Individual travertine beds attain a thickness of 0.3 to 7 m, while layers of clastic sediments vary from 0.5 m to 4 m in thickness. The entire thickness of this travertine–colluvium succession is ~24 m. In the upper part of the Chusang travertine (between ~250 m and ~330 m downslope of the modern main spring; Fig. 1C, D) at least five paleo-spring orifices, some up to 3 m in diameter and 2 m in height, are located. These orifices represent remnants of former travertine mounds and cones (Figs. 2B, 3A; Pentecost, 2005) and occur in the same stratigraphic horizon. Travertine sheets precipitated from water that discharged from these orifices, causing coalescing of the mounds and cones into an interconnected complex (Figs. 1D, 2A). Additional travertine mounds are present at Chusang but are less well-preserved. In south-eastern direction (i.e. upslope towards the human imprints and the modern main hot spring) further layers of travertine and colluvium are overlying this complex with the main modern hot spring discharging on top of this succession (Fig. 2A). Other travertine features such as larger slope terraces, travertine pools or dams are absent. Smaller terraces, mini-rimstone and shallow ponds exist but most of them suffered from surface erosion or are partly covered by clastic sediment.

3. Geological setting

The area of Chusang travertine is composed of a sequence of shallow-marine and clastic sedimentary rocks (limestone, sandstone and siltstone), as well as volcanic rocks (tuffaceous rocks, dacite, andesite and lava breccia). This sequence is known as Chaqupu Formation and extends from the Late Paleozoic into the Mesozoic (Zhang, 1997; Xie et al., 2010). Thin-section analysis of a sample obtained from the bedrock that underlies the Chusang travertine at its eastern margin yielded an oolite limestone, which according to Xie et al. (2010) is Triassic in age. The volcanic rocks occur stratigraphically and tectonically below these carbonates and thus likely constitute the deeper parts of the Chusang aquifer (Xie et al., 2010). Tectonically speaking, the study area is part of the Lhasa terrane and situated 27 km east of the Yadong-Gulu graben system (Armijo et al., 1986; Yin and Harrison, 2000), one of six approximately north–south striking graben systems

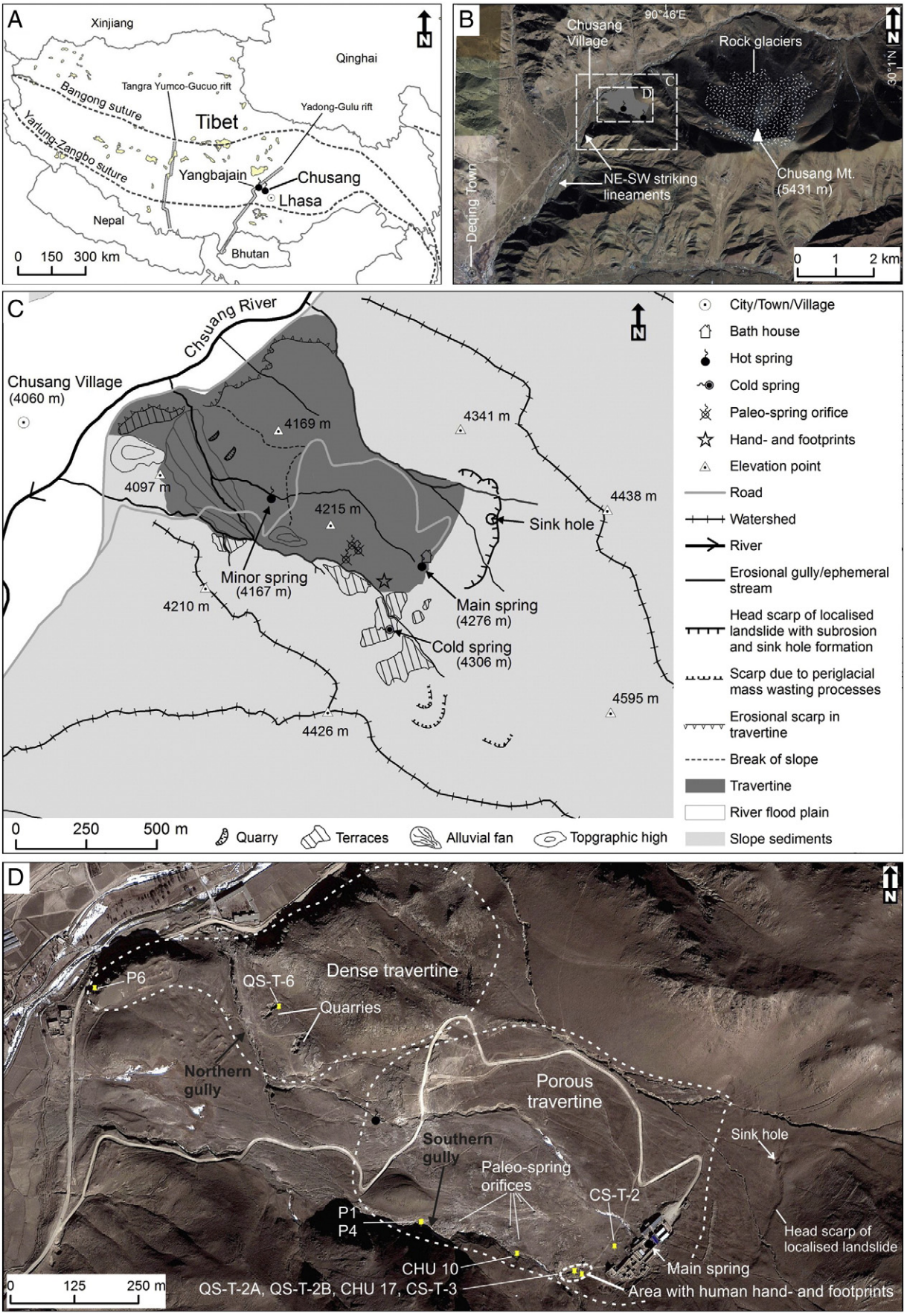

Fig. 1. Location of the Chusang travertine site (A) and its geomorphological setting (B and C) as well as sampling locations (D). Images B and D are from Google Earth.

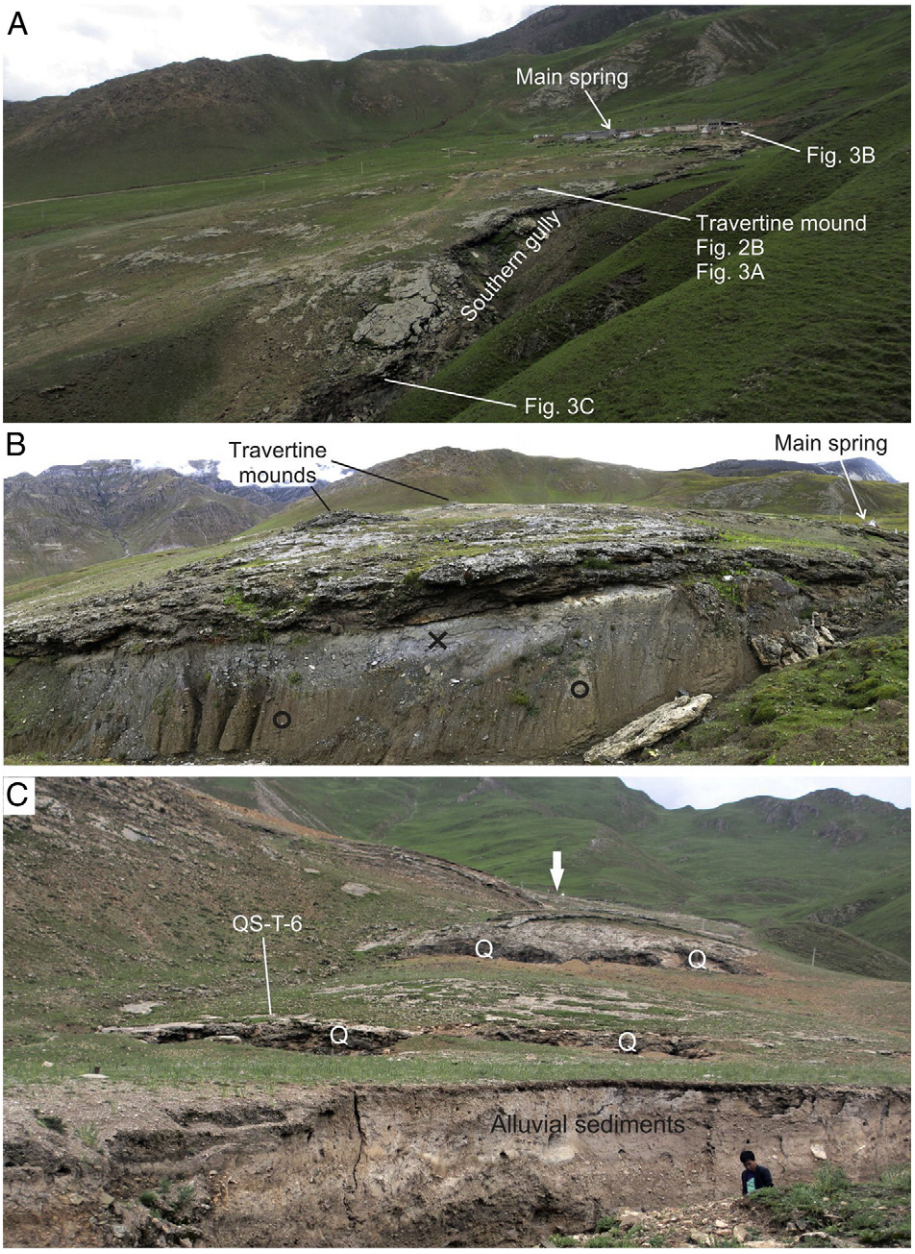

Fig. 2. Geomorphological details and sedimentary architecture of the Chusang travertine. (A) View of the stratigraphic upper part of the Chusang travertine–colluvium succession (towards northeast) showing laterally extensive travertine sheets with bathing house complex in the background. (B) View of colluvial layer overlain by a travertine mound complex (southern gully, depth 7–12 m — see Fig. 4; view towards north). The colluvium is composed of grayish (x) and brownish (o) debris-flow deposits. (C) View of the stratigraphic lower part of the succession composed of dense laminated carbonate (bathing house in background marked by an arrow; view towards southeast). Several quarries (Q) indicate mining activities of local population. Sample QS-T-6 was taken from the lower left quarry. Younger alluvial fan sediments that rest on top of travertine are exposed in the foreground.

in southern Tibet with a particularly high spreading rate (6.5 mm/year; Blisniuk et al., 2001; Chen et al., 2004). These grabens in conjunction with normal faults and rifts in northern Tibet and right-lateral strike slip motion along the Yarlung-Tsangbo suture and the Karakorum Jiali fault zone accommodate much of the extensional deformation of the Tibetan Plateau that occurred during the Late Cenozoic in response to ongoing north–south shortening of the Tibetan crust and mantle lithosphere (Blisniuk et al., 2001; Taylor et al., 2003; Chen et al., 2004). On the Tibetan Plateau, hydrothermal springs are mainly bound to such active extensional faults (Armijo et al., 1986; Ge et al., 2008; Tan et al., 2014). For example, more than two dozens of hot springs and geysers are lined up along the main axis of the Yadong-Gulu graben with several hydrothermal sites – including Chusang – in close proximity to this graben (Han, 1981). Based on satellite image studies of lineaments near Chusang village and extensional structures on the travertine itself (both oriented parallel to the Yadong-Gulu graben system; Fig. 1A, B), we assume that the Chusang hot spring, that is situated ~27 km east of the graben's main axis, is structurally associated with the Yadong-Gulu graben system.

4. Methods

Field investigations were carried out in the summers of 2012 to 2014. Geomorphological mapping in the field was aided by analysis of Google Earth imagery and logging of clastic sediment was based on the lithofacies codes of Eyles et al. (1983). In the field, water temperature, pH, electrical conductivity (EC) and alkalinity of the main and the minor springs were determined in summer 2012. Furthermore, water samples were collected from both springs for chemical analyses. The concentrations of the major cations in the spring water (i.e. Na^+,

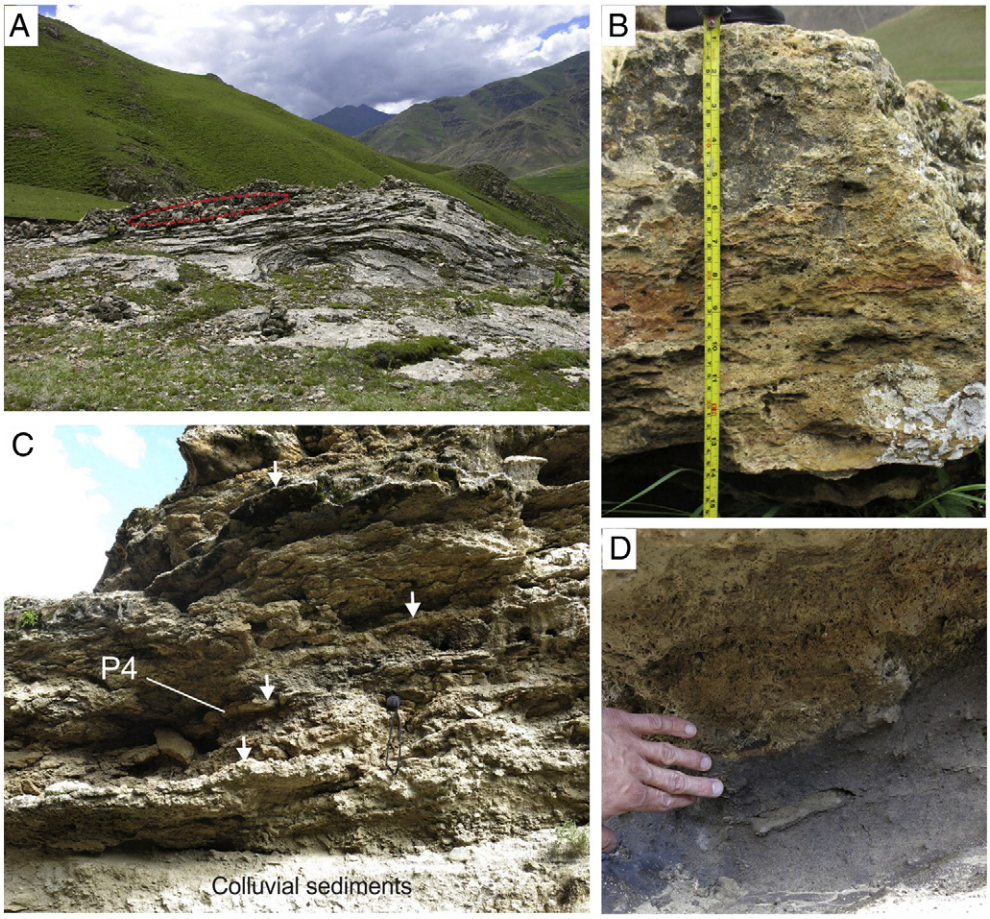

Fig. 3. Field images showing petrographic characteristics of the Chusang travertine. (A) Paleo-spring orifice ~250 m downslope of the modern main spring with a diameter of ~2 m (red dotted line). Note dense laminated travertine lithofacies dominates the proximal part of travertine mound. (B) The porous layered travertine lithofacies revealing yellowish to reddish surface staining. (C) Middle section of the southern gully (7–10 m depth, see Fig. 4; view towards north) is dominated by a travertine breccia interbedded with dense laminated travertine (10–30 cm in thickness; arrows). Sample P4 was obtained from such a dense laminated travertine layer in this outcrop. (D) Organic-rich colluvial layer overlain by porous travertine. (For interpretation of the references to color in this figure legend, the reader is referred to the web version of this article.)

K^+, Ca^{2+}, Mg^{2+}, Sr^{2+}) and Si were determined via inductively-coupled plasma optical emission spectrometry (ICP-OES). Cl^- and SO_4^{2-} concentrations were measured using ion chromatography. The saturation index with respect to calcite (SIcc) of the spring water was calculated using PHREEQC (Parkhurst and Appelo, 2013).

This study is based on 25 travertine samples that were cut in half and their macro-fabrics studied. For 20 samples with representative crystal fabrics thin sections were obtained and the position of the most representative samples (i.e. those that are also shown in the Figs. 5–8) is indicated in Fig. 1D. Microscopic crystal fabrics were examined under a Nikon Eclipse E400POL microscope using transmitted-light. This microscope is also equipped with an OSRAM HBO mercury short arc lamp to emit light in the UV spectrum (330–380 nm) for epifluorescence microscopy. The mineralogy of 37 sub-samples was determined via powder X-ray diffraction (XRD) analyses. Scanning electron microscope (SEM) analyses were performed on polished slabs, with a JEOL JSM-6010LV, operating at 15 kV at a working distance of 21 mm. Furthermore, selected micro-fabrics were analyzed using an electron microprobe (JEOL Superprobe 8100; analytical conditions: 15 kV acceleration voltage and 10 nA beam current) in order to (i) determine the elemental content of these fabrics and to (ii) generate elemental concentration maps for selected areas. A micro-X-ray fluorescence (μXRF) spectrometer (BRUKER Tornado M4) was used to acquire an element map 20 × 10 mm (1500 × 761 pixels) for one of the samples. The μXRF map has a spatial resolution of 13 μm/pixel (equals >50% beam overlap) and a chemical resolution of ~100 ppm.

Three samples were sub-sampled for uranium-series (i.e. ^{230}Th/U) dating: two travertine samples (QS-T-6 and P4) and one flowstone-like secondary calcite formed in travertine fracture (sample P6c; Fig. 1D). 5–15 mg calcite powders were obtained from each sample using a hand-held driller and a tungsten carbide drill bit. Chemical separation and purification of U–Th isotopes followed a modified protocols described in Hoffmann (2008). U and Th isotope measurements were undertaken using a ThermoFinnigan Neptune Multi-Collector Inductively Coupled Plasma Mass Spectrometer (MC-ICP-MS) following procedures outlined in Hoffmann et al. (2007). Activity ratios are calculated from isotope concentration ratios using decay constants according to Jaffey et al. (1971) (λ238), Cheng et al. (2000) (λ234 and λ230) and Holden (1990) (λ232). The ^{230}Th/U ages and their uncertainties (quoted at the 95% confidence level) are given in Table 1.

5. Hydrochemistry of the modern hot springs

The main hot spring has a year-round stable temperature of ~40–43 °C (Table 1; Zhang, 1997; Tong et al., 2000) with pH values between 6.0 and 6.6 (Table 2). Major ions (100–1000 mg/L) are HCO_3^-, Ca^{2+}, Cl^- and Na^+, whereas Mg^{2+}, K^+ and SO_4^{2-} are present at low concentrations only (<30 mg/L; Table 2). Concentrations of Li, Cs, B and Si were determined too, but only for the main spring, and found to be elevated (Tong et al., 2000; Table 2). The temperature of the minor spring is 23.0 °C, and thus ~19 °C lower than that of the main spring (Table 2). Despite this difference in water

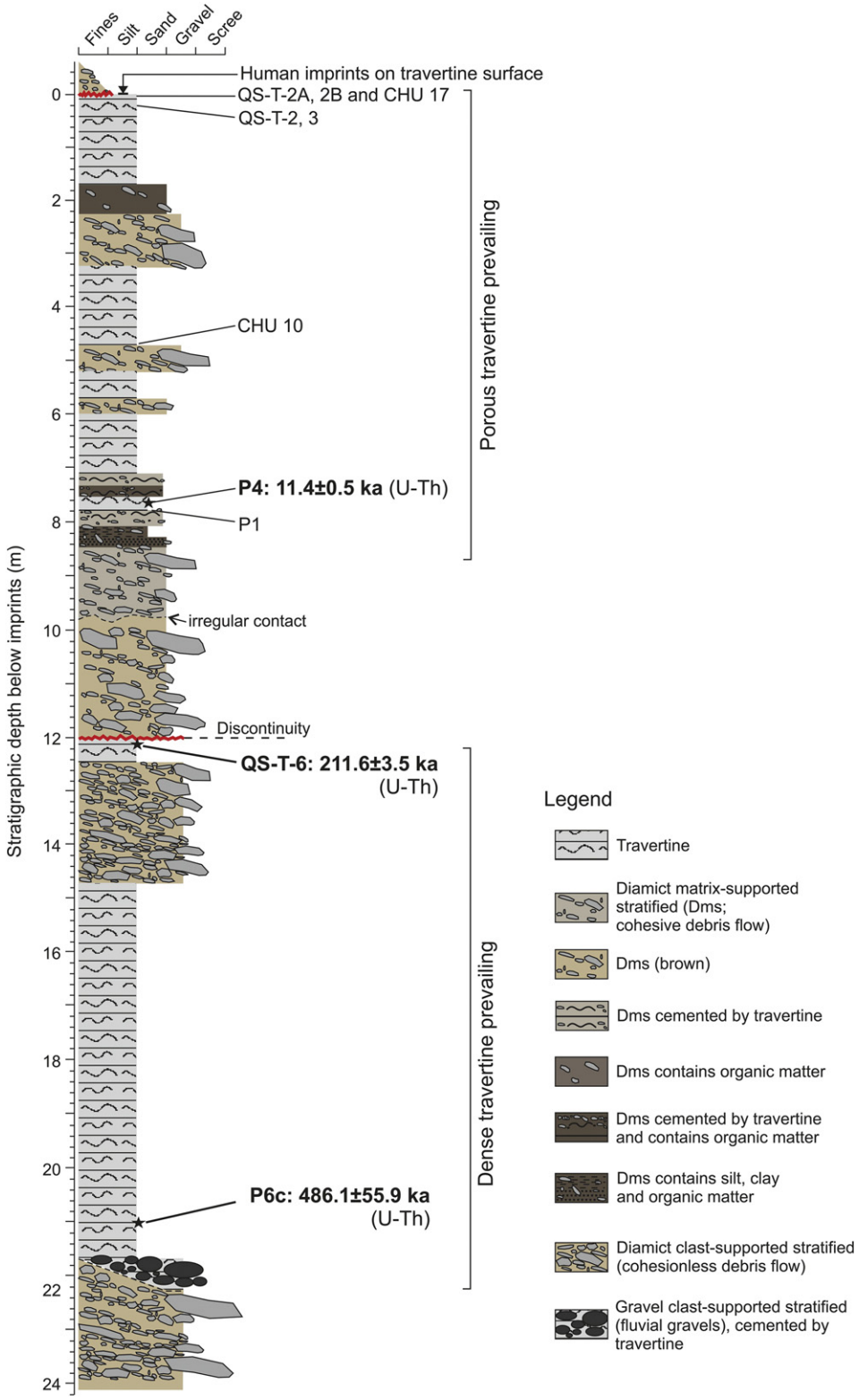

Fig. 4. Stratigraphic profile for the travertine–colluvium succession at Chuang and position of key-samples and ^{230}Th/U ages (compare Fig. 1D and Table 1). Note that the key-samples (n = 10, out of a total of 25 samples on which the whole study is based on) are also shown in the Figs. 5 to 8. The stratigraphic profile has been compiled from sedimentary logs obtained along erosional gullies that cut into the Chusang travertine (see Fig. 1D for location of gullies).

temperature, the hydrochemistry of both springs is very similar (Table 2). The SIcc values of both springs range from 0.1 to 0.4 (Table 2) and modern carbonate precipitation is restricted to the flow path of the hot spring water, where white carbonate crusts occur that are only a few cm in thickness.

6. Mineralogical and elemental composition

XRD and electron microprobe analyses suggest that the dominant mineral of the Chusang travertine is low-Mg calcite (~0.2 wt.% Mg concentration). Aragonite (up ~25–50%) was identified in the white pore

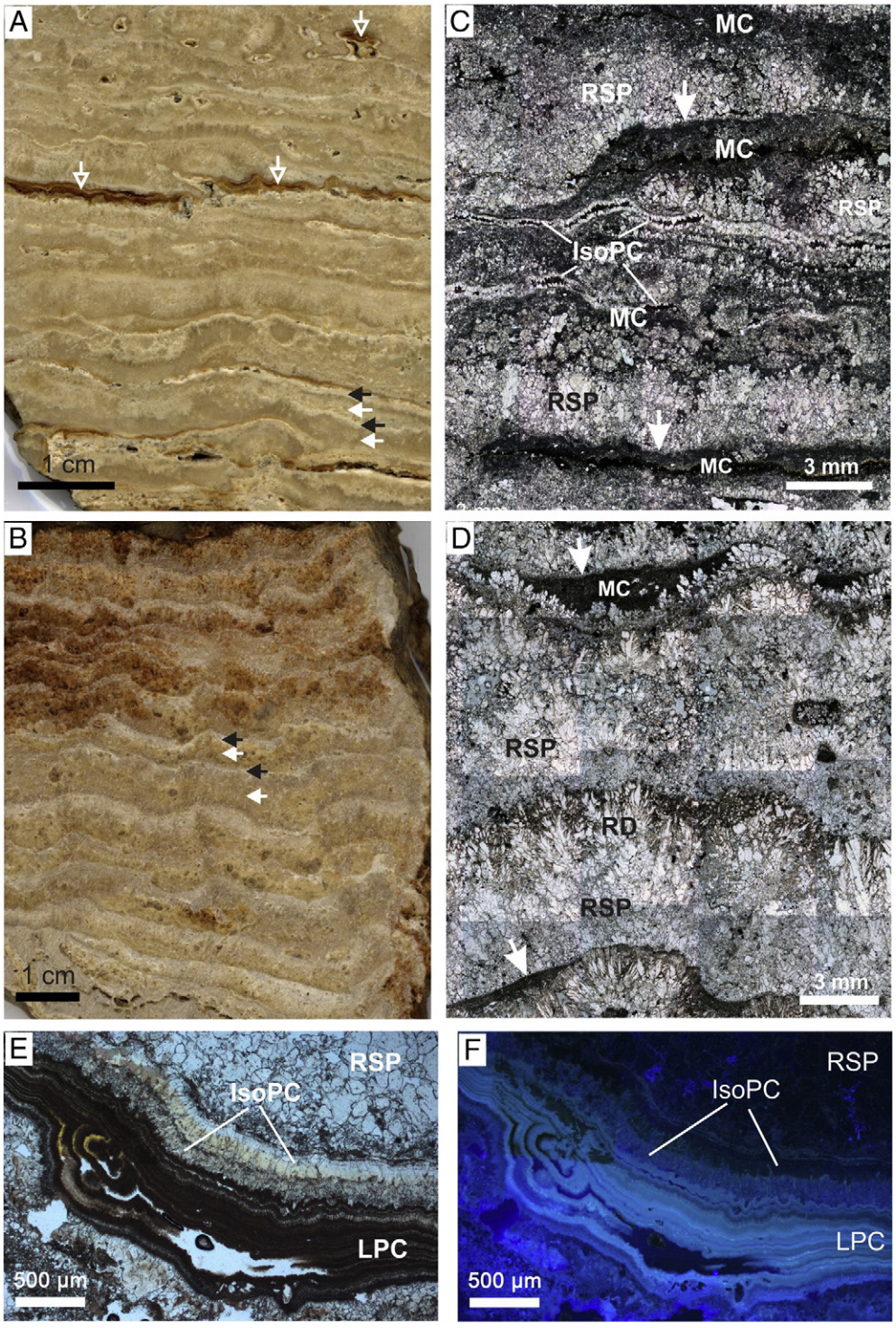

Fig. 5. Polished slabs (samples QS-T-6 (A) and P4 (B)), and photomicrographs of the dense laminated travertine lithofacies. (A, B) Dense laminated travertines showing lamination that is composed of brownish–yellowish laminae (white arrows) alternating with whitish laminae (black arrows). Note the dark brownish void-filling cement (white open arrows in A) and the reddish (i.e. weathered) laminae in the upper part of B. (C, D) The lamination in both samples QS-T-6 (C) and P4 (D) consists of thick laminae composed of dendrites (RD) that are partly or completely recrystallized to sparite (recrystallized sparite — RSP) and alternate with thin laminae composed of dark micrite (MC). Note the sharp upper contact of the MC laminae to the RSP (arrows in C, D) and isopachous scalenohedral sparitic pore cement (IsoPC in C). (E) Detail of dark brownish and laminated pore cement (LPC; also indicated with white open arrows in A). (F) Strong fluorescence in the LPC (same field of view as E), whereas the IsoPC shows little or no fluorescence. Images C–E taken in plane-polarized light; epifluorescence image F taken under UV stimulation. (For interpretation of the references to color in this figure legend, the reader is referred to the web version of this article.)

cement that occurs e.g. in sample QS-T-2A by XRD and electron microprobe mapping (detailed description below). Furthermore, a bulk travertine sample (140 g of sample CS-T-2) was dissolved in hydrochloric acid in order to determine the composition of its insoluble residue. XRD analyses showed that the acid-insoluble residue is composed of quartz, feldspar and mica constituting about ~20 wt.% of the bulk sample.

7. Description and interpretation of fabrics and lithofacies

Based on sedimentary logging, the investigation of cut hand specimen and thin-section petrography a range of lithofacies can be recognized within the Chusang travertine–colluvium succession, including (i) a dense laminated, (ii) a porous layered and (iii) a intraclastic

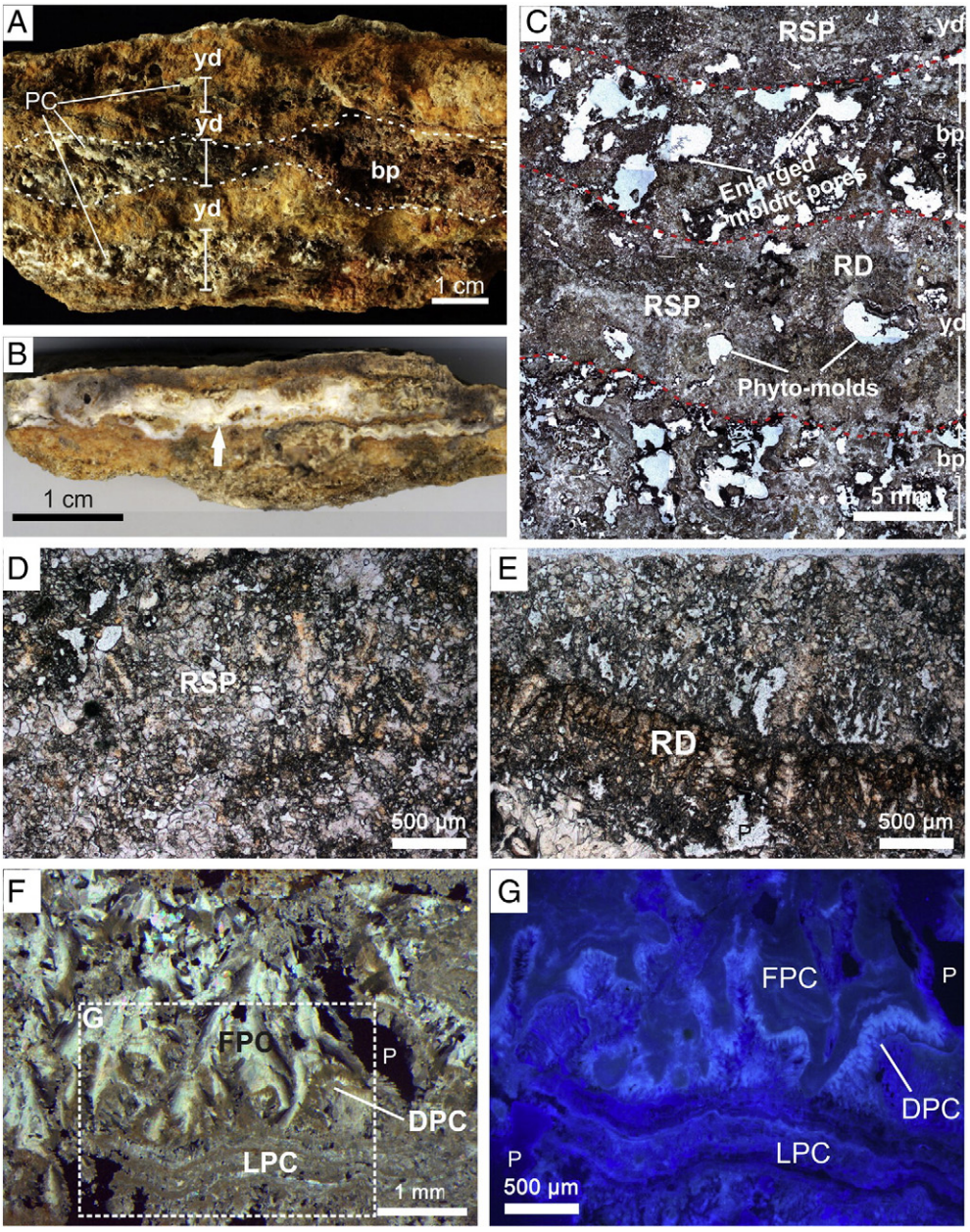

Fig. 6. Hand specimen (sample CHU 17(A)), polished slab (sample QS-T-2A (B)) and photomicrographs of the porous layered travertine lithofacies. (A, B) Porous layered travertines showing an alternation of cm-sized brown porous (bp) and yellowish dense (yd) travertine layers. Note the vadose pore cement (PC in A) composed of white fibrous crystals that preferentially occurs in the brown porous layers and an up to 5 mm-thick layer of dense white pore cement that fills a laterally extensive pore (arrow in B). (C) Photomicrograph showing cm-scale alternation of porous and relatively denser travertine layers in sample CHU 17. Dashed lines indicate the layer boundaries. The dense travertine layers are mainly composed of recrystallized sparite (RSP in D), but often preserve relict dendrites (RD in E). The porous layers are characterized by abundant moldic pores, resembling phyto-molds and often show evidence for enlargement by dissolution. Note that a few phyto-molds also occur in the dense calcite layer (C). (F) Several generations of pore cement occur in the porous layers of sample QS-T-2A, including fibrous pore cement (FPC), laminated pore cement (LPC), and dendritic pore cements (DPC). The FPC consists of large fibrous crystals (D). These fibrous crystals show undulose extinction. The DPC covers the fibrous and laminated pore cements and the growth direction is always oriented downward into the pore space. All cement generations are fluorescent, with the fluorescence signal of the DPC being particularly strong (G). Images C–E taken in plane-polarized light; image F taken in cross-polarized light; epifluorescence image G taken under UV stimulation. (For interpretation of the references to color in this figure legend, the reader is referred to the web version of this article.)

travertine lithofacies, as well as (iv) a debris-flow facies comprising colluvial and alluvial sediments. The bedding geometry and thickness along with the (macro- and micro-) fabrics, porosity and diagenetic features that characterize these lithofacies are introduced in the following and summarized in Table 3.

7.1. Dense laminated travertine lithofacies

The dense laminated lithofacies forms lenticular to tabular beds that vary in thickness from 5 to 30 cm and are always inclined (~5–30°) and mostly dipping downslope (Fig. 3A, C). This lithofacies has low porosity (≤5 vol.%) and – on the meso-scale – is characterized by wavy but laterally continuous lamination that is composed of brownish–yellowish laminae (~2–4 mm in thickness) that alternate with thin whitish laminae (~0.5–1 mm in thickness; Fig. 5A, B).

Microscopically, the thick brownish–yellowish laminae are composed of branching calcite crystals that are up to ~6 mm long and grew (sub) perpendicularly to the substrate (Fig. 5C, D). These crystals morphologically resemble the "feather dendrites" of Jones and Renaut (1995) or the "cedar-tree crystals" of Kitano (1963) and are thus

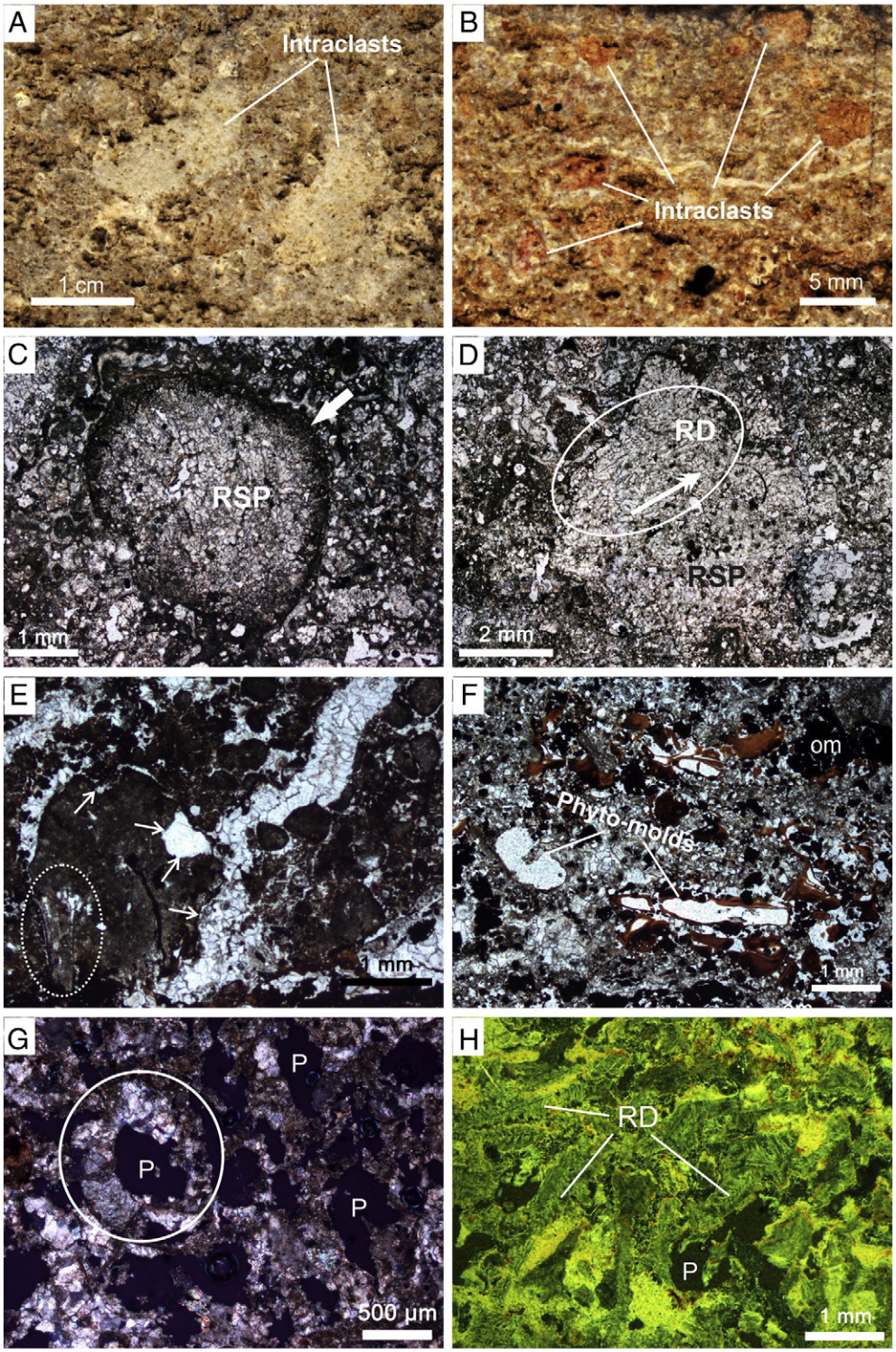

Fig. 7. Polished slabs (sample CS-T-2 (A) and sample CS-T-3 (B)) and photomicrographs of the intraclastic travertine lithofacies. (A) Large whitish sub-round travertine intraclasts (up to 2 cm in size). (B) Small brownish sub-rounded intraclasts (~2–5 mm). (C) Detail of a well-rounded intraclast covered by a thin micrite envelope (arrow). This intraclast is composed of recrystallized sparite (RSP), forming an equant mosaic. (D) Detail of a sub-angular intraclast that preserves relict dendrites (RD). Arrow indicates the growth direction of the dendrites. (E) Intraclastic travertine (sample CHU 10) mainly composed of dark, well-rounded micrite intraclasts (0.5–2 mm). Note a large micritic intraclast in lower left-hand corner showing evidence of dissolution (arrows) and containing a large bioclast (circle). (F) Phyto-molds and brownish clay coatings observed in an intraclastic travertine (sample P1). Note the pore-filling opaque peloids composed of organic matter (om). (G) Moldic pores surrounded by sparite (circle). (H) Relict dendrites (RD) that are up to several mm in length and show variable growth directions are interpreted as subaqueous in origin (sample CS-T-3, see also Fig. S4). Images C–F taken in plane-polarized light; image G taken in cross-polarized light; image H taken in cross-polarized light and dark field illumination. (For interpretation of the references to color in this figure legend, the reader is referred to the web version of this article.)

referred to as dendrites. In many cases dendritic crystals have recrystallized into coarse-grained and bladed spars arranged in a mosaic but the original morphology of the main branches of the former dendrite crystals can still be discerned (Fig. 5C, D). The thin whitish laminae are composed of dark micrite that is usually recrystallized into microsparite (Fig. 5C, D). These microsparitic laminae overlay the dendritic laminae with a sharp contact (Fig. 5C, D). Both, the dendritic and micritic laminae lack fluorescence upon UV stimulation.

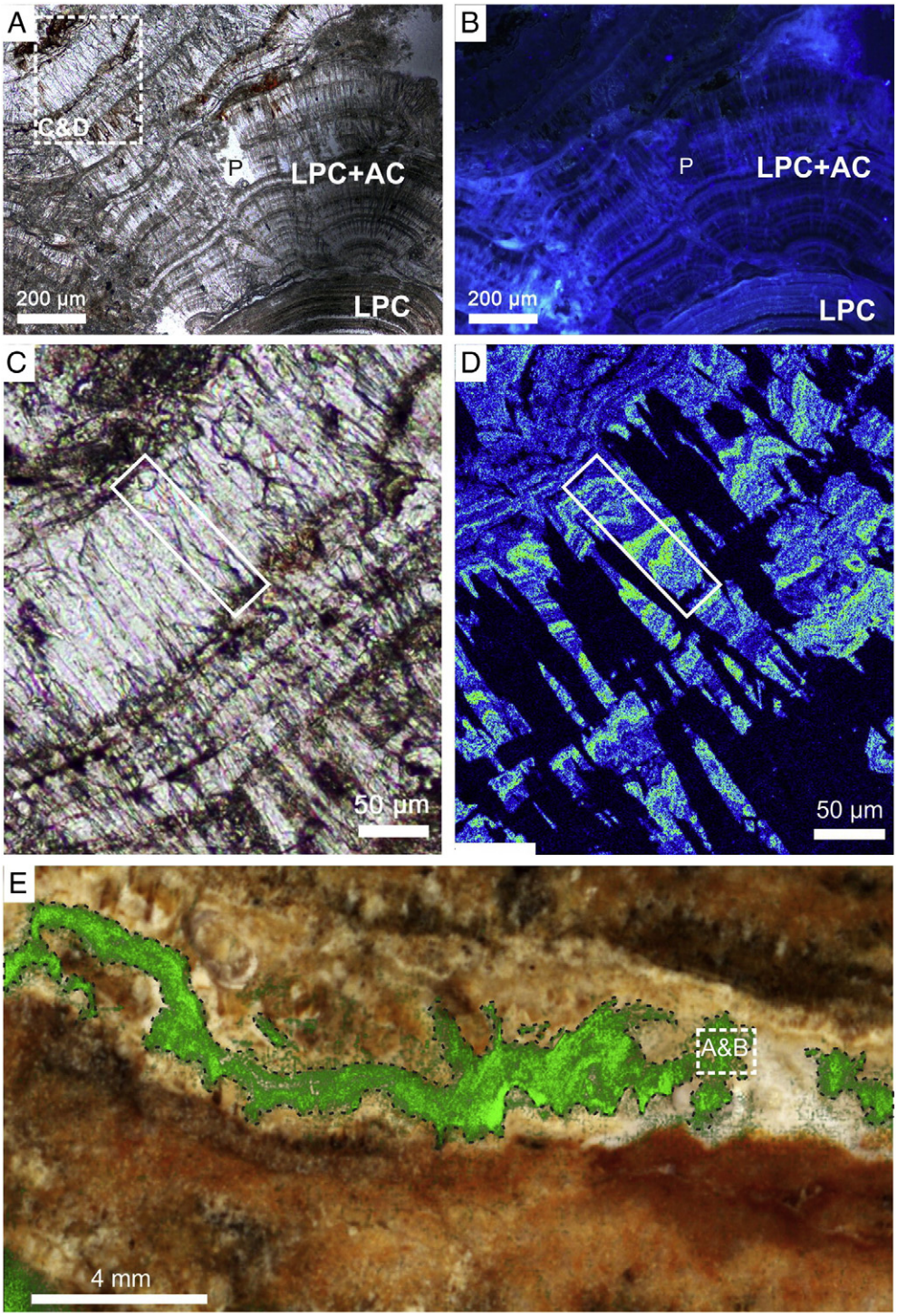

Fig. 8. Petrographic details of the laminated pore cement (LPC) in the travertine sample QS-T-2A. (A) Intergrowth of acicular crystals with laminated calcite. The lamination is composed of translucent sparitic layers alternating with brown micrite laminae. The acicular crystals originate from a nucleation point situated in the lower right-hand corner of the image and grew towards the upper left-hand corner of the image forming crystal bundles. Note that the lamination tightly follows the curvature of these aragonite crystal bundles. (B) The acicular crystals showing strong fluorescence. (C, D) Microprobe mapping reveals that the translucent sparitic layers (white rectangle in (C, D)) are composed of distinct layers of high (yellow) and low (blue) Mg concentrations. The acicular crystals show very little Mg (dark blue) but elevated Sr concentrations (not shown). (E) The μXRF analyses confirm the presence of Sr in the LPC (green), but also highlight that Sr is not uniformly distributed in the LPC. Images A and C taken in plain-polarized light; epifluorescence image B taken under UV stimulation; images D and E are the microprobe and the μXRF mappings, respectively. (For interpretation of the references to color in this figure legend, the reader is referred to the web version of this article.)

7.1.1. Interpretation

Crystalline dendrites are a common abiotic fabric in travertines and form as a result of fast calcite precipitation from highly supersaturated water driven by rapid degassing of CO_2-rich water (Jones and Renaut 1995; Jones et al., 2000, 2005; Jones and Renaut, 2008). We infer the same mechanism as the main driving force for the formation of the thick dendritic laminae of the dense laminated lithofacies at Chusang. Formation of micrite is commonly associated with microbial mediation, resulting in clotted, peloidal and/or shrub micrites (Chafetz and Folk, 1984; Pedley, 1992; Gandin and Capezzuoli, 2014), but abiotic micrite

Table 1
Uranium and thorium concentrations, activity ratios and corrected U–Th ages for the Chusang travertine. Corrections for detrital contamination for individual subsamples assumed a value of 0.8 ± 0.4 for the $^{238}U/^{232}Th$ activity ratio of the detrital component (Wedepohl, 1995). Uncertainties are reported at the 95% confidence level.

Sample	Fabric	^{238}U	^{232}Th	$[^{230}Th/^{232}Th]$	$[^{232}Th/^{238}U]$	$[^{230}Th/^{238}U]$	$[^{234}U/^{238}U]$	Age (ka)	$[^{234}U/^{238}U]_{initial}$
		(ng/g)	(ng/g)	Activity ratio	Activity ratio	Activity ratio	Activity ratio	Corrected	Activity ratio
P4	Dendritic	497.59 ± 37.96	35.44 ± 2.69	9.22 ± 0.14	0.02328 ± 0.00005	0.215 ± 0.004	1.985 ± 0.007	11.4 ± 0.5	2.036 ± 0.0122
QS-T-6	Dendritic	205.78 ± 3.46	8.47 ± 0.15	80.19 ± 0.54	0.01345 ± 0.00008	1.079 ± 0.005	1.208 ± 0.003	211.6 ± 3.5	1.382 ± 0.0051
P6c	Columnar	227.78 ± 2.54	12.08 ± 0.14	59.24 ± 0.27	0.01734 ± 0.00004	1.028 ± 0.005	1.029 ± 0.003	486.1 ± 55.9	1.116 ± 0.0151

formation has been reported too (Jones and Renaut, 2008; Jones and Renaut, 2010). The micrite laminae of the dense laminated lithofacies lack biogenic features, both under transmitted light microscopy (Fig. 5) and SEM (Figs. S1A–C), suggesting that these micrite laminae might have formed via abiotic processes too. The general lack of-fluorescence in this lithofacies indicates the absence of organic compounds, in-line with abiotic calcite precipitation from hot spring water. Both, dendrites and micrite are often affected by early diagenetic alteration, causing partial or complete transformation of dendrites into a mosaic of sparite, while micrite often recrystallized into microsparite (Love and Chafetz, 1988; Jones and Renaut, 2008).

In travertines the alternation of dendritic layers with thin micritic bands commonly indicates (i) a seasonal control of travertine growth (e.g. seasonal variation in air temperature) and/or (ii) cyclic changes in flow velocity and flow pattern of the spring water (Jones et al., 2005; Pentecost, 2005; Jones and Renaut, 2008). Based on observations from Clinton travertine in British Columbia (Canada), Jones and Renaut (2008) provide a model of the control mechanism that leads to a dense laminated travertine lithofabric similar to that observed at Chusang. At the Clinton travertine site thick laminae composed of dendrites formed as long as the discharge and the calcite supersaturation are high enough to sustain fast (dendritic) calcite precipitation (i.e. during spring and summer). Strong cooling during winter and/or burial of the spring site beneath ice and snow (at least in the distal parts where the water temperature has cooled down sufficiently) reduced the amount of degassing and decreased the level of supersaturation, thus causing the SIcc to drop below a critical threshold impeding dendritic calcite formation (SIcc <2–5; Jones et al., 2000; Jones and Renaut, 2008). Similarly, snow and ice or partial freezing of spring water will dampen the turbulent nature of the water outflow and also prohibit rapid CO_2 degassing and thus dendritic calcite formation (Jones and Renaut, 2008). According to Jones and Renaut (2008), thin bands of abiotic micrite – termed growth lines – can form during these seasonal halts of dendrite growth and mark peak winter conditions. In this model the strong seasonality and semi-arid climate is driving the cyclic alternation of dendritic and micritic laminae (in the Clinton region winter temperatures are as low as −37 °C and summer temperatures as high as 40 °C; Jones and Renaut, 2008). Similar cyclicity in dendrite growth is also known from the travertine deposits at Lýsuhóll, Iceland (Jones et al., 2005), where, low temperatures in combination with snow and ice accumulation during winter months have been responsible for annual pauses in dendrite growth as well (Jones et al., 2005). The occurrence of growth lines in the dense laminated lithofacies at Chusang (Fig. 5C, D) and the overall similarities to the lithofacies described by Jones et al. (2005) and Jones and Renaut (2008) suggest that this model might also be applicable in a Tibetan context, where winters are known to be particularly cold and dry and summers comparatively mild and wet (winter temperatures at Chusang can attain −20 °C and summer temperatures 25 °C; based on data of the Public Weather Service Center of China).

7.2. Porous layered travertine lithofacies

High porosity (~20–40%) and cm-scale layering characterize this lithofacies on the meso-scale. The layering is composed of brown porous calcite layers that are ~1–2 cm thick and that alternate with yellowish relatively denser calcite layers that are ~0.5–1 cm thick (Fig. 6A, B). On the outcrop-scale this lithofacies reveals sub-horizontal tabular bedding with undulated contacts and individual beds that are 10–40 cm in thickness (Fig. 3B). The porous layered travertine lithofacies prevails in the stratigraphically upper section of the Chusang travertine–colluvium succession (0–8 m depth in Fig. 4).

Two main types of microscopic crystal fabrics are present in this lithofacies: (1) recrystallized sparite (RSP; Fig. 6D) and (2) dendrites that are recrystallized and preserved as relicts only (relict dendrites — RD; Fig. 6E). The recrystallized sparite is composed of transparent, equant crystals forming mosaics. Such mosaics are common in both, the yellowish dense and the brown porous travertine layers (Fig. 6C; Figs. S2, S3). Dark micrite fills most intercrystalline pores (Fig. 6D). Neither the sparites nor the micrite shows fluorescence upon UV stimulation. The relict dendrites are confined to the yellowish dense layers and are (i) either recrystallized into a sparite-like mosaic but with the main branches and the first-order sub-branches still preserved (Fig. 6E); or (ii) strongly recrystallized and only the main branches of former dendrites are discernable (Fig. 6D; Figs. S2, S3). Originally, none of these dendrites has been longer than ~1–2 mm, and most dendrites were even much smaller (~200–500 μm). The relict dendrites are sometimes reddish to brownish stained (e.g. Fig. 6E), but lack fluorescence.

Pores are widespread in the porous layered travertine lithofacies and are mostly 1–10 mm in size. Most pores have irregular shapes, but regular pores that morphologically resemble phyto-molds and fenestral pores can be observed too and are particularly common in the brown porous layers (Fig. 6C; Fig. S2). Furthermore, evidence of enlargement of these existing pores due to dissolution exists, often blurring the origin of these pores (Fig. 6C; Fig. S2).

7.2.1. Interpretation

We invoke abiotic and fast calcite precipitation for the relict dendrites encountered in the yellowish dense layers (Jones et al., 2005; Jones and Renaut, 2008), i.e. the same process as for the dendrites of the dense laminated lithofacies. However, the relict dendrites of the

Table 2
Chemical compositions of the Chusang hot springs. The data of 1975 and 1989 are from Zhang (1997) and Tong et al. (2000).

	Discharge (L/s)	T (°C)	pH	EC (μS/cm)	Na (mg/L)	K (mg/L)	Ca (mg/L)	Mg (mg/L)	Sr (mg/L)	Li (mg/L)	Cs (mg/L)	Cl^- (mg/L)	SO_4^{2-} (mg/L)	HCO_3^- (mg/L)	Si (mg/L)	B (mg/L)	SIcc
Main spring (1975)	1	43.0	6.40	843	135.0	18.8	110.0	21.1	–	1.3	0.8	126.0	21.5	620.0	20.5	13.0	−0.09
Main spring (1989)	0.1	42.2	6.00	927	162.0	28.5	140.0	21.5	–	1.4	2.1	120.0	2.14	635.0	30.8	12.5	−0.40
Main spring (2012)	0.1–0.3	40.0	6.55	1606	142.3	22.4	196.2	21.5	1.7	–	–	148.2	4.0	902.8	16.4	–	0.38
Minor spring (2012)	0.1–0.3	23.0	6.58	1508	138.4	21.6	169.2	23.2	1.7	–	–	130.7	6.2	866.2	16.4	–	0.13

Table 3
Description and interpretation of different lithofacies recognized in the Chusang travertine–colluvium succession.

Lithofacies	Bedding geometry and thickness	Fabrics	Porosity	Diagenetic features	Interpretation of fabrics	Depositional environment and distribution of lithofacies
Dense laminated travertine	Lenticular to tabular with sub-parallel contacts; 5–30 cm	*Dendrites*: 1.5–6 mm long, occasionally forming fan-shaped aggregates; *micrite*: precipitated as thin laminae on top of dendrites partly infilling intercrystalline pores; *lamination*: 2–4 mm thick dendritic laminae alternate with 0.5–1 mm thin micritic laminae; micritic laminae overlay dendritic laminae with a sharp contact; UV[a]: no fluorescence	≤5 vol.%; *intercrystalline pores* (0.005–0.5 mm); *framework pores* (1–2 mm); *elongated pores* parallel to lamination (≤1 mm thick)	*Recrystallized sparite* (RSP): coarse-grained and bladed spars arranged in a mosaic; *pore cements*: isopachous (IsoPC), laminated (LPC) UV: medium to strong fluorescence for LPC	*Dendrites*: deposited by highly supersaturated hydrothermal water via rapid CO_2 degassing (i.e. fast abiotic calcite precipitation; Jones et al. 2005); *lamination*: caused by cyclic (likely seasonal) changes in climate and/or spring discharge rate, *micrite laminae* interpreted as winter layers (Jones and Renaut, 2008); *recrystallized sparite*: sparite-like mosaic via aggradational neomorphism (Love and Chafetz, 1988); *pore cements*: preferential in lower part of the succession (12–22 m depth[b]); precipitated under vadose (LPC) and phreatic (IsoPC) conditions in laterally extensive pores formed by dissolution (Pentecost, 2005);	Smooth slopes, relative proximity to travertine mounds and cones; lithofacies prevails in lower part of the succession (12–22 m depth[b]); interbedded with porous layered and intraclastic travertine
Porous layered travertine	Tabular with undulating contacts; 10–40 cm	*Relict dendrites* (RD): ~200–500 μm long, prevailing in the dense layers, partly stained; *micrite* filling intercrystalline pores; *layering*: ~1 to 2 cm thick very porous layers (micritic and/or recrystallized) alternate with ~0.5–1 cm thin relatively denser (dendritic) layers; UV: no fluorescence	20–40%; *intercrystalline pores* (0.005–0.05 mm) *moldic pores* (2–10 mm); *fenestral pores* (0.5–2 mm);	*Recrystallized sparite* (RSP): coarse-grained and bladed spars arranged in a mosaic *enlarged pores* due to dissolution; *pore cements*: fibrous (FPC), laminated (LPC) and dendritic (DPC) UV: strong fluorescence for FPC, LPC and DPC	*Relict dendrites*: deposited by supersaturated hydrothermal water via CO_2 degassing (i.e. slow abiotic calcite precipitation; Jones et al., 2005); *recrystallized sparite*: sparite-like mosaic via aggradational neomorphism (Love and Chafetz, 1988); *moldic and fenestral pores*: dominate in the porous layer, probably result from the decay of e.g. encrusted macrophytes and algal mats (Heimann and Sass, 1989; Pentecost, 2005); *porous layers*: indicate high biological productivity thus interpreted as summer layers *pore cements*: mainly precipitated via (re)infiltration of hot spring water and mixing with rain water, vadose conditions (Pentecost, 2005);	Low relief topography; lithofacies prevails in the upper part of the succession (0–8 m depth[b]) e.g. in shallow depressions and ponds behind mounds; interbedded with dense and intraclastic travertine
Intraclastic travertine	Lenticular to tabular with sub-parallel contacts; 10–50 cm	*Intraclasts* 0.3–20 mm in diameter, sub-angular to well-rounded, composed of recrystallized sparite (RSP), *relict dendrites* (RD) or micrite and microsparite; thin *micrite envelopes* surround intraclasts; *other allochthones*: opaque peloids (0.1–0.4 mm), detrital grains (e.g. quartz, feldspar) *travertine breccias*: cm to dm, angular clasts UV: no fluorescence, exception: some micritic intraclasts with medium to strong fluorescence	10–20%; *intercrystalline pores* (0.005–0.05 mm); *moldic* and *fenestral* pores (0.5–2 mm);	*Recrystallized sparite* (RSP): coarse-grained and bladed spars arranged in a mosaic; *enlarged pores* due to dissolution; *pore cements*: laminated (LPC), dendritic (DPC); UV: medium to strong fluorescence for LPC and DPC	*Intraclasts* derived from erosion of pre-existing lithified travertine mainly via frost weathering (Sanders et al., 2010); *allochthones*: input of terrigenous (e.g. quartz, feldspar) and organic matter (organic peloids) e.g. via soil erosion and slope wash processes *recrystallized sparite*: sparite-like mosaic via aggradational neomorphism (Love and Chafetz, 1988); *pore cements* mainly precipitated via (re)infiltration of hot spring water and mixing with rain water, vadose conditions (Pentecost, 2005);	Distal gentle slopes and depressions/ponds, distal parts of travertine mounds; lithofacies prevails in upper part of the succession (0–8 m depth[b]); interbedded with dense and porous layered travertine
Debris flow	Massive layers, no bedding; irregular contacts; 50–300 cm	Matrix-supported diamict; (sub-)angular clasts (≤20 cm); silty matrix with shear planes; microscopic organic material	n.a.	n.a.	*Cohesive debris flows* caused by soil erosion, slope wash and/or periglacial slope processes (Blikra and Nemec, 1998; Nemec and Kazanci, 1999; French, 2007)	Proximal to hillslopes, thinning distally; interbedded with travertine (at least 7 colluvial layers[b])

[a] UV: stimulation with UV light (330–380 nm; i.e. epifluorescence microscopy).
[b] Compare Fig. 4.

porous layered lithofacies are smaller by an order of magnitude compared to dendrites from the dense laminated lithofacies, suggesting that abiotic calcite precipitation was slower in the porous lithofacies. The lack of fluorescence in the relict dendrites indicates an absence of organic compounds in their crystal lattice, which is in agreement with an abiotic origin of this fabric. Recrystallization (aggradational neomorphism) allowed a sparitic mosaic to form that still resembles the dendritic fabric (Love and Chafetz, 1988; Jones and Renaut, 2008).

Compared to the yellowish dense layers the brown porous layers suffered from a higher degree of diagenetic overprinting (recrystallization, dissolution enlargement of pores and precipitation of pore cements). Hence, the formation of these layers is more difficult to decipher, but a biological origin is likely, as outlined in the following. Chafetz and Folk (1984) and Chafetz and Guidry (1999) stated that biological influence becomes significant on travertine precipitation in gradually more distal or lower energy environments. In such distal settings organisms, such as bacteria (particularly cyanobacteria), algae, mosses and reeds can induce and/or influence carbonate precipitation through (i) metabolic process, such as photosynthetic CO_2 removal which increases carbonate saturation and/or (ii) the role played by biofilms and mats as substrates for crystal nucleation (Pentecost, 1995; Fouke et al., 2000; Dupraz et al., 2009; Rainey and Jones, 2009; Fouke, 2011; Della Porta, 2015). Neither transmitted-light microscopy nor SEM analysis on recrystallized sparites of the porous layered travertine lithofacies provides additional clues regarding the importance of biological influence on travertine precipitation. SEM images from the porous layered lithofacies rather confirm that early diagenetic modifications are pervasive and blur the origin of these fabrics (Figs. S1D–I).

We are thus left with the observations that (i) moldic pores in travertines as those observed in the porous layered lithofacies are often interpreted as phyto-molds, i.e. biotic structures that resulted from encrustation and subsequent decay of biological material (e.g. leaves, twigs, weeds, mosses and algae; Heimann and Sass, 1989; Pentecost, 2005); and (ii) fenestral pores are usually caused by the inclusion of gas bubbles but can also be associated with algal mats (Pentecost, 2005).

The relatively large size and high concentration of moldic and fenestral pores in the porous brown travertine layers (Fig. 6C; Fig. S2) suggest that these layers might be associated with enhanced biological activity during the summer months (Heimann and Sass, 1989; Pentecost, 2005; Rainey and Jones, 2009). We envisage that biological material such as algae and other (water) plants acted as nucleation points and/or removed CO_2 via photosynthesis from the water column thus facilitating calcite precipitation, but decayed thereafter, which is in-line with the general lack of fluorescence in the recrystallized sparite that forms the brownish calcite layers. This interpretation is sensible, because during Tibetan summers enhanced monsoon precipitation and higher temperatures stimulate biological activity. Furthermore, mixing of rain and spring water occurs during the summer months as well, thus diluting and cooling hydrothermal water, which in turn favors the growth of biota (Guo and Riding, 1998). We further suggest that the dense yellowish layers that are dominated by relict dendrites represent abiotic travertine precipitation outside the monsoon season (i.e. from October to May). From autumn onward decreasing temperature and increasing dryness slow down or even prohibit mixing of hydrothermal water with rainwater, which in turn slows down and eventually stops organism growth, allowing small abiotic dendrites to form. This process should be particularly important in low-relief areas where ponding of hydrothermal and rain water occurs (Guo and Riding, 1998).

7.3. Intraclastic travertine lithofacies

This lithofacies forms lenticular to tabular beds with undulating contacts and thicknesses between 10 and 40 cm (Fig. 3C). Travertines from this lithofacies contain abundant sand- to gravel-sized (up to 20 mm in diameter) intraclasts derived from erosion of pre-existing travertine (Guo and Riding, 1998; Rainey and Jones, 2009; Gandin and Capezzuoli, 2014). These intraclasts are whitish and sometimes brownish in color and most intraclasts are sub-rounded to well-rounded, but sub-angular intraclasts occur as well (e.g. Fig. 7A, B). Also belonging to this lithofacies type are travertine breccia layers (~30–50 cm thick) that are composed of centimeter to decimeter-sized angular travertine clasts (Fig. 3C). These layers are clast-supported and some are blackish in color suggestive of a high organic content and/or the presence of oxidized manganese.

On the microscopic scale, the travertine intraclasts are mainly composed of recrystallized sparites (Fig. 7C), but some intraclasts preserve recrystallized dendrites too (Fig. 7D). Most of these intraclasts are surrounded by a thin, irregular dark micrite envelope (Fig. 7C, D). In some samples intraclasts are composed of dark brown micrite and/or microsparite (e.g. Fig. 7E). Some of these intraclasts even show a complex internal structure, i.e. consist of multiple calcite clasts, contain calcified bioclasts, show several generations of micrite envelope and/or evidence for dissolution. Only some micritic intraclast as well as the calcified bioclasts show medium to strong fluorescence.

Moldic and fenestral pores with diameters of 0.5–2 mm are present in the intraclastic travertine lithofacies (Fig. 7F, G; Fig. S4). Furthermore, corroded dendrites arranged in a relatively loose network and showing variable growth directions are sometimes preserved and sealed by layers of intraclastic travertine (e.g. sample CS-T-3; Fig. 7H; Fig. S4). In addition, small opaque peloids (50–150 μm in diameter) are present in some samples (e.g. Fig. 7F). These peloids either fill pore spaces or are dispersed in a sparitic carbonate matrix or between micrite clasts and show little fluorescence. Furthermore, pores (including phytomolds) are often coated with finely laminated brownish sediment, suggestive of clay coatings (Fig. 7F). Quartz and feldspar grains as well as clay pebbles are present in this lithofacies too, but are not abundant.

7.3.1. Interpretation

Several studies have shown that intraclasts in travertines are derived from erosion of lithified travertine deposited in the upstream area and deposition in depressions or ponds (Guo and Riding, 1998; Rainey and Jones, 2009; Gandin and Capezzuoli, 2014). Erosion of spring carbonates typically occurs in slope or waterfall settings during high discharge events (Guo and Riding, 1998), but in a cold and periglacial setting such as Chusang frost weathering might also significantly contribute to travertine erosion and thus intraclast formation (cf. Sanders et al., 2010).

The sorting of the intraclasts is generally poor in all samples and in combination with the pre-dominant sub-rounded grain morphology this suggests short transport distances. Furthermore, intraclasts with a complex internal structure (dissolution features, several generations of micrite envelopes, composed of multiple intraclasts, contain calcified bioclasts) point towards a complex sedimentation history with multiple cycles of erosion and deposition including dissolution and cementation, at least for some intraclasts. The opaque peloids are most likely organic matter (and possibly contain also manganese oxides; Stoops, 2003; Rennert et al., 2014) that (i) entered the sediment cascade and were transported and deposited as peloids, or (ii) were washed into the intraclastic travertine at a later stage and filled the pores. Finally, clay infiltrated into these travertine beds, forming laminated pore coatings that also drape opaque peloids.

All these micro- and macroscopic observations suggest that the intraclastic travertine lithofacies indicates gentle slopes or distal depressions and/or ponds, where clastic sediment accumulation dominated. The intraclastic lithofacies thus broadly resembles the lithoclastic travertine facies of Guo and Riding (1998). This interpretation is in-line with the observation of corroded dendrites that are arranged in a relatively loose network with variable growth directions and that are overlain by several layers of intraclastic travertine. We interpreted these dendrites as subaqueous in origin, i.e. the expression of a local pond (Fig. 7H; Fig. S4) into which intraclastic travertine was deposited.

7.4. Debris flow facies

The sedimentary logs in Fig. 4 show that colluvial sediment constitutes a significant proportion of the Chusang deposit (~9.5 m or ~40% of the log in Fig. 4). Most of these clastic layers are matrix-supported diamicts, with angular to sub-angular clasts typically up to 20 cm in

size embedded in a silt matrix that locally reveals shear planes (Dms; Fig. 4). Some colluvial layers contain abundant (mostly microscopic) organic material (Fig. 3D) and cementation of clastic sediment by carbonate can also be observed (Figs. 3C, 4). One of the thickest colluvial layers (8.4–12 m depth, Fig. 4) reveals an internal sedimentary zonation: grayish sediment that tends to be slightly carbonate-cemented overlays – with an irregular contact – loose brownish slope-wash sediment (Fig. 2B).

7.4.1. Interpretation

The matrix-supported diamicts containing angular to sub-angular clasts as well as the presence of shear planes suggest that these clastic sediments are cohesive debris flows sourced from the adjacent hillslopes (Blikra and Nemec, 1998; Nemec and Kazanci, 1999). Croci et al. (2016) described colluvial fan deposits interbedded with travertine and concluded that the colluvial fan deposits resulted from debris flows triggered by occasional rainstorms. Significant mass-wasting processes can be expected in a periglacial setting like Chusang, with a catchment reaching in elevation from ~4200–4900 m asl., slopes that are 20°–30° steep and characterized by a sparse vegetation cover and subjected to intensive freeze–thaw weathering (French, 2007). We thus infer that the colluvium interbedded into the travertine is ultimately linked to slope wash and/or periglacial slope processes on the adjacent slopes.

7.5. Pore cements

In the dense laminated travertine lithofacies intercrystalline pores and framework pores occur (Fig. 5D), but most of these pores are healed due to widespread recrystallization. In this lithofacies prominent cements only occur in lower stratigraphic positions (i.e. 12–22 m depth; Fig. 4), where they are bound to ~1 mm-thick pores that are up to several centimeters long and extend parallel to the lamination (Fig. 5A). In hand specimens these cements are brown in color (Fig. 5A). Microscopically they are either isopachous (IsoPC; isopachous fibrous or scalenohedral sparitic with thicknesses of 100–300 μm; Fig. 5C) or laminated (LPC, composed of alternating micritic and sparitic laminae, each ~20 μm in thickness; Fig. 5E). Only the laminated pore cement shows bright fluorescence upon UV stimulation (Fig. 5F).

In the porous layered travertine lithofacies cements are more widespread (particularly in the brown porous layers) and often contain white dense calcite cements that – on the macroscopic scale – are either forming micro-stalactitic crystals that grew downward into the pores (Fig. 6A) or are finely laminated (Fig. 6B). On the microscopic scale at least three types of pore cements are recognized: fibrous, laminated and dendritic. The same three types of pore cements also occur in the intraclastic travertine lithofacies.

The fibrous pore cement (FPC) is composed of large fibrous crystals. These crystals are 0.5–1 mm in length, grew downward into the pore space and reveal an irregular outline (Fig. 6F, G; Fig. S3). The FPC shows undulose extinction under crossed nicols and weak fluorescence (Fig. 6F).

The dendritic pore cement (DPC) is dark brownish under transmitted-light and reveals strong fluorescence upon UV stimulation (Fig. 6F, G; Fig. S3). This cement generation either forms a thin (~0.1–0.5 mm) veneer covering pre-existing calcite fabrics (e.g. secondary fibrous crystals) or fills pores (Fig. 6F; Fig. S3). The dendritic crystals always grew downward into the pores.

The laminated pore cement (LPC) can attain a thickness of several mm (Figs. 6B, 8E; Fig. S3) and is composed of translucent sparitic laminae (~15–40 μm in thickness) interbedded with thin, brown micrite laminae (~5–20 μm; Fig. 8A). The brown micritic laminae show strong fluorescence, while the sparitic laminae are non-fluorescent (Fig. 8B). This laminated fabric is cross-cut by acicular crystals that are arranged in radiating bundles resembling aragonite (Fig. 8A). In transmitted-light and epifluorescence it can also be observed, that (i) these acicular crystal bundles start radiating from a nucleation point, (ii) the lamination follows the curvature of these bundles, and that (iii) areas composed of laminated fabric only exist as well (Fig. 8A, B). Element mapping reveals that the translucent calcite layers are composed of alternating high and low Mg micro-bands, while the Sr concentration is generally low (Fig. 8C, D). The acicular crystals, in contrast, reveal very low Mg but elevated Sr concentrations (e.g. Fig. 8C, D). The μXRF analysis shows that elevated Sr concentrations (indicative of aragonite) are not uniformly distributed in this pore cement and that the white pore cement is partly Sr-poor (Fig. 8E). Samples for XRD drilled from such areas of laminated pore cement also showed no aragonite.

7.5.1. Interpretation

Pore cement in travertines can be directly precipitated by infiltrating spring water, while direct rain and soil-percolation water will preferentially cause surface dissolution and re-precipitation (i.e. karstification; Pentecost, 2005). In many instances mixing of hydrothermal and rain water will occur thus reducing the degree of supersaturation and in combination with the geometry of the pore space determine the type of pore cement. If hot spring water highly supersaturated with respect to calcite percolates the travertine, cement precipitation in the form of dendritic fabrics might be expected.

In the dense laminated travertine lithofacies pore cements occur in laterally extensive pore spaces usually confined to the micrite layers. These pores are probably caused by dissolution or fracturing of the laminated travertine, with the micrite layers being a preferential fracture plane or horizon of dissolution. The pores were subsequently filled by isopachous pore cement precipitated under phreatic conditions followed by laminated pore cement that formed under vadose conditions (Fig. 5C, E). The bright fluorescence of the laminated pore cement suggests that this cement is precipitated from percolation water that also carried humic and fulvic acids (McGarry and Baker, 2000).

In several large pores of the porous layered lithofacies a sequence of at least three cement generations separated by dissolution events can be observed: The oldest cement in the porous layered travertine lithofacies is the fibrous cement that grew from the top of the pores downward and shows clear signs of corrosion (Fig. 6F; Fig. S3). Subsequently, the laminated cement formed, which was affected by corrosion as well (Figs. 6F, 8A, B; Fig. S3). Finally a dendritic cement generation is locally present that covers the fibrous and laminated cements (Fig. 6F; Fig. S3). Particularly bright fluorescence is associated with this youngest cement generation, suggesting that hot spring water containing dissolved humic and fulvic acids infiltrated into the porous travertine deposit during a relatively late diagenetic stage. Continuing hydrothermal activity linked to spatio-temporal variability of hot water flow paths during travertine accretion is a reasonable explanation for repeated infiltration of hydrothermal water into the travertine deposit causing precipitation of dendritic pore cement.

An interesting detail of the LPC is that it shows an intergrowth of laminated calcite with acicular crystals. The morphology of these acicular crystals as well as the very low Mg but elevated Sr concentrations measured in these crystals suggest that these needles are composed of aragonite (Fig. 8C, D; Pentecost, 2005). XRD analysis conducted on sub-samples taken from this intergrown fabric confirmed the presence of aragonite. XRD analysis from areas that lack such an intergrowth (i.e. are laminated and Sr poor based on μXRF mapping) yielded calcite but no aragonite. This suggests that in the LPC calcite–aragonite intergrowths and laminated calcite that lacks such intergrowths are co-existing, which is supported by transmitted-light and epifluorescence microscopy (Fig. 8A, B). Furthermore, the fact that the lamination follows the curvature of the aragonite crystal bundles implies that calcite laminae precipitated essentially synchronously with the formation of aragonite crystal bundles (Fig. 8A, B). In sum these observations point towards a co-precipitation of aragonite and calcite rather than diagenetic replacement of aragonite by calcite (Guo and Riding, 1992; Folk, 1994; Frisia and Borsato, 2010; see the

supplementary material for a discussion of the specific geochemical boundary conditions).

8. Discussion

8.1. Depositional concept and facies model

We synthesize our geomorphological, sedimentological and petrographical observations into a depositional concept and facies model, graphically represented in Fig. 9.

At 4235 m asl. and 250 m downslope of the modern hot spring a complex of travertine mounds developed on top of a thick colluvial layer that provided a ~10° dipping paleo-surface on which the travertine precipitated (Fig. 2B). These mounds are composed of dense laminated travertine (Fig. 3A), and the overall geometry of these mounds is asymmetric (Fig. 9A, B): at the downslope side the travertine dips initially at ~30°, but after a few meters flattens out and gradually attains the local hillslope angle of ~10° (Fig. 2B). The downslope extent of travertine sourced from these orifices can exceed 100 m. Because these mounds form on an inclined surface, accretion against the upper slope is limited by mound height (Figs. 3A, 9B). At Chusang these travertine mounds and slopes are dominated by dense laminated travertine and fit the smooth slope facies of Guo and Riding (1998), where dense crystalline crusts composed of dendritic calcite crystals reflect rapid precipitation under high flow rates.

The distal parts of the travertine mounds are dominated by porous travertine of the intraclastic travertine lithofacies and travertine breccia. Dense laminated travertine layers can be intercalated with the intraclastic travertine facies (Fig. 3C). In our depositional model (Fig. 9B) the intraclastic travertine lithofacies results from travertine mound collapse and/or break-up of adjacent travertine slope deposits, while the spring orifices are still active (indicated by the intercalation of dense laminated travertine), resulting in cementation and mixing of intraclastic travertine with in-situ precipitates. This interpretation is in line with sedimentological observations from several other tufas and travertine sites, where erosion and brecciation of travertine slopes and cones caused accumulation of lithoclast travertine at distal slopes and local depressions (Guo and Riding, 1998; Pellicer et al., 2014; Pola et al., 2014). Furthermore, pre-existing colluvium might become partly cemented while travertine mounds are prograding downslope and mixing of intraclastic travertine with colluvium can also occur (Figs. 2B, 3C).

While travertine mounds aggradate and eventually combine into larger complexes, flats and local depressions form on top of mounds and behind mound complexes. In our model the growth of travertine mounds on an evenly inclined hillslope mantled with colluvium will thus result in an undulating terrain with areas of low topography that favor ponding. The gentle topography also facilitates the development of the porous layered travertine lithofacies observed at Chusang (Fig. 9A, B) via the following processes: (i) reduced flow velocity of hot spring water that results in precipitation of thin calcite layers composed of small dendrite crystals (i.e. yellow dense layers; Fig. 6A, C; Fig. S2), and (ii) dilution of hot spring water by rain water that increases organic growth (e.g. algae, mosses, and grasses) and allows encrustation and biologically influenced travertine precipitation (formation of porous brown layers with moldic and fenestral pores, Fig. 6A, C; Fig. S2). As outlined above, we expect rain water availability and biological productivity, and thus the succession of yellow dense and brown porous calcite layers at Chusang to be mainly controlled by seasonality. According to our depositional model this lithofacies should thus be particularly common in shallow depressions or on gentle slopes where the flow of hot spring water is low and seasonally modulated by rainfall (Fig. 9B) and is broadly comparable to the marsh-pool facies of Guo and Riding (1998). Furthermore, if local growth geometries allow ponds to form that are entirely feed by hydrothermal water with no or only little input of rain or soil-percolation water (at least temporarily), sub-aqueous dendrites develop (Fig. 7H; Fig. S4). Clastic sediment input into these depressions is also common and thus porous layered travertine or subaqueous dendrites are frequently interbedded with colluvium and intraclastic travertine sourced from adjacent hillslopes or travertine mounds (Fig. 9B; Fig. S4). Periodically drying of these shallow depressions and gentle slopes results in weathering and staining (sample QS-T-2A, Fig. S3; sample CS-T-3, Fig. S4; Guo and Riding, 1998).

Fig. 9C depicts a facies succession based on our petrographic observations and the facies distribution model outlined above. In this schematic diagram deposition of dense travertine on a slope or travertine mound grades into porous layered travertine (due to the changing relief while the travertine slope propagates and the mound flattens), followed by the precipitation of subaqueous dendrites (development of local ponds fed by hot spring water behind a growing mound complex) and accumulation of intraclastic travertine (from an adjacent travertine mound and/or hillslope; Fig. 9C). Finally, percolating rain and hot spring waters induce diagenetic alterations, including recrystallization of dendritic fabrics and dissolution of pre-existing travertine and precipitation of pore cements (Fig. 9C). The latter process is particularly common in the porous layered travertine lithofacies. The last generation of pore cements of the porous travertine lithofacies is composed of small dendrites, indicating that hot spring water was still flowing from the travertine mounds and (repeatedly?) infiltrated this lithofacies. This observation suggests that travertine formation and early diagenetic alteration (i.e. cementation) can be broadly contemporaneous.

8.2. Age constraints and sedimentary evolution

Several aspects of the Chusang travertine render ^{230}Th/U dating problematic: (i) the widespread recrystallization of primary fabrics likely resulted in open-system behavior and thus gain or loss of radionuclides; (ii) recrystallization might have caused mixing and intermingling of different crystal fabrics of different isotopic composition; and (iii) many calcite samples likely contain unsupported ^{230}Th (i.e. detrital contamination). Given these challenges a precise ^{230}Th/U chronology will probably not be achievable for the porous layered and clastic travertine lithofacies, where porosity and detrital contamination are high and recrystallization is ubiquitous. Nevertheless, it is expected that careful subsampling of primary fabrics, such as well-preserved dendrites from the dense laminated lithofacies, will yield reliable ^{230}Th/U dates. In order to obtain a first chronological framework for the colluvium–travertine succession at Chusang we obtained two samples showing well-preserved dendrites from the dense laminated lithofacies from ~7.6 m and ~12.2 m depth (sample P4 and QS-T-6, respectively; Figs. 1D, 4) and one flowstone-like secondary calcite from ~21 m depth that formed in a travertine crack (sample P6c; Figs. 1D, 4). The results are given in Table 1 and suggest that the base of the travertine–colluvium succession has a minimum age that dates into the Middle Pleistocene, while the sample from 7.6 m depth yielded an Early Holocene age.

These (preliminary) ages in combination with our facies model provide insights into the sedimentary evolution of the travertine–colluvium succession at Chusang. Travertine spring orifices are known to shift temporally and spatially because travertine cones and mounds frequently self-seal due to the rapid deposition of travertine at the

Fig. 9. Depositional concept and facies distribution model of the Chusang travertine. (A) Plan view of travertine mounds that merge into mound complexes via lateral and downslope progradation and are influenced by contemporaneous debris-flow activity. (B) Schematic cross section along section A–A′ showing the development of travertine mound complexes and the distribution of the travertine facies. (C) Petrographic facies model. For both, the dense laminated and the porous layered lithofacies travertine precipitation is likely controlled by seasonality (for details see text).

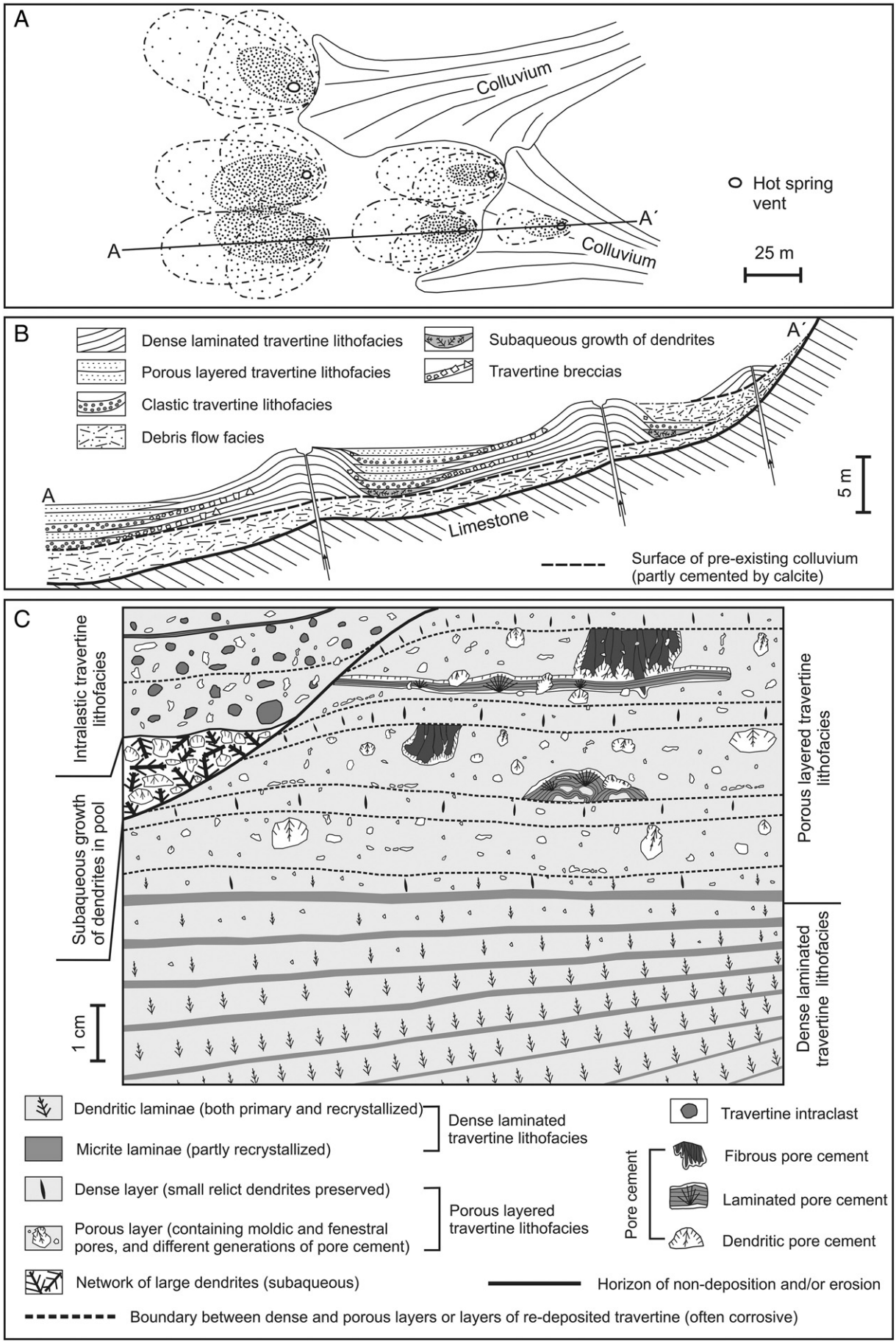
A
Colluvium
A´
A
Colluvium
Hot spring vent
25 m
B
Dense laminated travertine lithofacies
Porous layered travertine lithofacies
Clastic travertine lithofacies
Debris flow facies
Subaqueous growth of dendrites
Travertine breccias
A´
A
Limestone
5 m
Surface of pre-existing colluvium (partly cemented by calcite)
C
Intralastic travertine lithofacies
Subaqueous growth of dendrites in pool
Porous layered travertine lithofacies
Dense laminated travertine lithofacies
1 cm
Dendritic laminae (both primary and recrystallized)
Micrite laminae (partly recrystallized)
Dense laminated travertine lithofacies
Dense layer (small relict dendrites preserved)
Porous layer (containing moldic and fenestral pores, and different generations of pore cement)
Porous layered travertine lithofacies
Network of large dendrites (subaqueous)
Travertine intraclast
Pore cement
Fibrous pore cement
Laminated pore cement
Dendritic pore cement
Horizon of non-deposition and/or erosion
Boundary between dense and porous layers or layers of re-deposited travertine (often corrosive)

surface or within the throat of hydrothermal spring vents (Pentecost, 2005; Capezzuoli et al., 2014). Today, the main active hot spring at Chusang emerges at 4270 m asl. on top of the travertine–colluvium succession (Figs. 1, 2). The early Holocene travertine sample P4 from 7.6 m depth precipitated from a paleo-spring orifice at ~4212 m asl. that merged with several other travertine mounds and cones that were active at the same time into a laterally extensive travertine sheet (Fig. 2A, B). Older orifices existed further downslope but are morphologically not well preserved; i.e. they must have been situated at ~4113 m asl. ca. 211 ka ago (sample QS-T-6; Fig. 2C) and at ~4074 m asl. ca. ≥486 ka ago (sample P6c; at the level of the modern Chusang river). These data suggest a lateral shift of the hot spring vent system by ~1 km into southeastern direction over the course of the last ca. 500 ka (Fig. 1).

A characteristic feature of the Chusang travertine is the interbedding of travertine and colluvium and this interbedding becomes more common in the stratigraphic upper part of the studied succession (Fig. 4). We attribute this general increase of terrigenous sediment input – at least partly – to the fact that the shift of the hot spring vent system towards southeast was also accompanied by (i) vertical aggradation of the travertine deposit and (ii) an increase in the proximity of the hot spring mounds and cones to the nearby hillslopes, which in turn facilitated hillslope processes to interact with hydrothermal carbonate precipitation. The bulk of the colluvium was deposited by cohesive debris flows which sometimes contain organic matter that originates from entrained soil and vegetation of the adjacent hillslopes (Fig. 3D). Because the travertine sheets (particularly the dense laminated lithofacies) are relatively resistant to erosion these sheets also protect the underlying colluvial sediment and thus preserve old terrigenous strata that can contain a biological signal from the former hillslopes.

8.3. Paleoclimatic controls

Over centennial to orbital timescales hydrothermal activity and thus travertine deposition is chiefly affected by (i) tectonics allowing hot spring vent systems to open or close and thus influencing deep groundwater circulation (Hancock et al., 1999; Brogi and Capezzuoli, 2009; Brogi et al., 2016) as well as (ii) climate which is a fundamental controlling factor on the hydrology and thus on groundwater recharge (Pentecost, 2005; Viles and Pentecost, 2007). In many instances the development of hydrothermal systems and travertine deposits have been linked to humid climatic phases (Faccenna et al., 2008; De Filippis et al., 2013; Croci et al., 2016). For the Tibetan Plateau it is well established that the Indian summer monsoon (ISM) delivers the bulk of atmospheric precipitation (Tian et al., 2001) and that the intensity of the ISM fluctuated over millennial to orbital timescales in response to insolation changes (Cai et al., 2010, 2015; Zhu et al., 2015; Kathayat et al., 2016). Isotopic studies from Tibet further suggest that (i) hydrothermal spring water is mainly recharged via atmospheric precipitation and that (ii) groundwater circulation on the plateau is rapid and thus residence times for hydrothermal water are short (i.e. a few decades; Tan et al., 2014). For the Tibetan Plateau it would thus be reasonable to expect phases of strong ISM and travertine precipitation to be synchronous, albeit the role of tectonics (e.g. earthquake recurrence cycles) has to be considered too (Brogi and Capezzuoli, 2014; Brogi et al., 2014; Gradziński et al., 2014).

Climate is also widely recognized as a principal control on colluvial sedimentation, and especially humid climatic conditions (e.g. heavy rainfall) are often triggering debris-flows (Blikra and Nemec, 1998; Nemec and Kazanci, 1999). However, in high-altitude areas an increase in air temperature might induce permafrost degradation and enhance snow-melt runoff and thus also stimulate debris-flow activity (Damm and Felderer, 2013). For Tibet it can be suspected that intensive bedrock weathering of the hillslopes under periglacial conditions (e.g. freeze–thaw cycles) results in a thick slope cover (French, 2007), which in combination with a sparse vegetation cover makes these hillslopes prone to mass-wasting processes. We argue that this preconditioning of the hillslopes in conjunction with an enhanced ISM is likely to cause slope erosion as well as colluvial and alluvial valley aggradation over millennial time scales.

Today, no significant debris-flow activity is evident in the Chusang (or in any neighboring) catchment, and erosion is confined to (i) the headward erosion of small gullies and (ii) periglacial slope processes such solifluction, and small-scale active-layer detachment slides at altitudes >4400 m asl. (Fig. 1C, D). Modern hot spring activity is similarly sluggish, with very low discharge (~0.1–0.3 L/s) and only little modern hydrothermal carbonate precipitation. The presence of extensive colluvial sediment layers interbedded with travertine is thus in stark contrast to modern sedimentary processes and hot spring discharge. The sedimentary record at Chusang rather suggests that (i) precipitation of hydrothermal carbonate and erosional processes on the hillslopes were broadly synchronous and (ii) significantly higher in the past (Figs. 4, 9A). We further argue that an enhanced ISM is a plausible driving mechanism for both, travertine precipitation and colluvial sedimentation and thus a possible explanation to reconcile these sedimentological observations.

9. Summary and conclusions

The Chusang travertine is a ~24 m-thick sequence composed of hydrothermal carbonate interbedded with colluvium (mainly cohesive debris-flow layers) sourced from the surrounding hillslopes. Geomorphological mapping combined with logging suggests that hot spring water was discharged via travertine mounds onto a ~10° dipping paleo-slope mantled by colluvium. Growth of these travertine mounds is dominated by lateral and downslope progradation, causing individual mounds to merge. This growth mechanism results in an undulating terrain composed of multiple mounds forming a laterally extensive travertine sheet and ultimately controls the occurrence and distribution of the various travertine lithofacies, that include (i) a dense laminated, (ii) a porous layered and (iii) an intraclastic travertine lithofacies. Micro-fabric analyses suggest that the dense laminated travertine lithofacies preserves a cyclic signal that is likely seasonal in nature (i.e. abiotic dendritic calcite precipitation is interrupted during peak winter conditions allowing a thin band of micrite to from). The precipitation of the porous layered travertine lithofacies is cyclic as well and in our interpretation records seasonality via a biologically influenced calcite layer that forms during the monsoon season when both, rainwater availability and temperatures are high, allowing dilution of hot spring water and growth of biota (while abiotic dendritic calcite precipitation dominated during the rest of the year).

Diagenesis is ubiquitous in the Chusang travertine, but never alters the original crystal fabrics completely. The most common diagenetic processes include aggradational neomorphism resulting in mosaic-like fabrics composed of recrystallized sparite, and the extensive formation of pore cements that precipitated from infiltrated hot spring and/or rainwater. Most prominent is a generation of white laminated calcite cement that is in parts intergrown with acicular aragonite crystals. Petrographic and geochemical analyses reveal that both polymorphs formed almost coevally and did not suffer from diagenetic alteration.

Preliminary ^{230}Th/U dating suggests that the base of the travertine–colluvium succession at Chusang dates into the Middle Pleistocene, while the top ~8 m of the succession started accumulating in the earliest Holocene. A ~1 km shift of the hot spring orifices from the valley floor into southeastern direction and onto the adjacent hillslopes can be reconstructed from these ^{230}Th/U data and also explains the general increase of colluvial sediment input into travertine system with time.

Today debris flow activity and travertine precipitation are insignificant at Chusang, but the occurrence of large fossil travertine mounds and the interbedding of travertine with thick layers of debris-flows suggests that terrigenous and chemical sediment depositions were (i) orders of magnitudes higher in the past compared to today and

(ii) likely synchronous and therefore (iii) probably controlled by the same climatic forcing mechanism. We hypothesize that intervals of strong monsoon enhanced hydrothermal water circulation and travertine precipitation, as well as intensified slope processes and concomitant accumulation of colluvium at hillslope toes.

Our study shows that the Chusang travertine–colluvium succession may bear a ~500 ka record of paleoclimatic and paleoenvironmental change. Further dating efforts are required to constrain (i) the exact duration of individual pulses of travertine precipitation and colluvial sedimentation, as well (ii) the age for the human imprints encased in the top-most travertine sheet. We suggest that ^{230}Th/U dating of primary dendritic fabrics and of selected clean pore cements and luminescence dating of detrital-rich travertine as well as radiocarbon dating of organic rich colluvium are viable ways forward to obtain a high-resolution record from this unique site. Although likely discontinuous in nature, this sediment succession thus holds the potential to become one of the longest records for Quaternary paleoenvironmental change on the Tibetan Plateau.

Supplementary data to this article can be found online at http://dx.doi.org/10.1016/j.sedgeo.2016.07.002.

Acknowledgements

We thank Peter Tropper and Thomas Angerer (University of Innsbruck, Austria) for the assistance with microprobe and μ-XRF analyses, respectively. We are grateful to Licheng Shen, Yuchuan Sun, Kunyu Wu and Peng Wang (Southwest University, China) for their field assistance. Diethard Sanders (University of Innsbruck) is thanked for his assistance in petrographic analyses and discussion and Christoph Spötl (University of Innsbruck) for improving a previous version of this paper. We also thank two anonymous reviewers for their constructive comments. This study was supported by the Austrian Science Fund (FWF grant 24924-G19 to MCM) and the China Scholarship Council (CSC fellowship 2011699003 to ZW).

References

Andrews, J.E., 2006. Palaeoclimatic records from stable isotopes in riverine tufas: synthesis and review. Earth-Science Reviews 75 (1–4), 85–104.
Armijo, R., Tapponnier, P., Mercier, J.L., Han, T.L., 1986. Quaternary extension in southern Tibet — field observations and tectonic implications. Journal of Geophysical Research-Solid Earth and Planets 91 (B14), 13803–13872.
Ashley, G.M., Dominguez-Rodrigo, M., Bunn, H.T., Mabulla, A.Z.B., Baquedano, E., 2010. Sedimentary geology and human origins: a fresh look at Olduvai Gorge, Tanzania. Journal of Sedimentary Research 80, 703–709.
Blikra, L.H., Nemec, W., 1998. Postglacial colluvium in western Norway: depositional processes, facies and palaeoclimatic record. Sedimentology 45 (5), 909–959.
Blisniuk, P.M., Hacker, B.R., Glodny, J., Ratschbacher, L., Bi, S.W., Wu, Z.H., McWilliams, M.O., Calvert, A., 2001. Normal faulting in central Tibet since at least 13.5 Myr ago. Nature 412 (6847), 628–632.
Brogi, A., Capezzuoli, E., 2009. Travertine deposition and faulting: the fault-related travertine fissure-ridge at Terme S. Giovanni, Rapolano Terme (Italy). International Journal of Earth Sciences 98 (4), 931–947.
Brogi, A., Capezzuoli, E., 2014. Earthquake impact on fissure-ridge type travertine deposition. Geological Magazine 151 (6), 1135–1143.
Brogi, A., Capezzuoli, E., Martini, I., Picozzi, M., Sandrelli, F., 2014. Late Quaternary tectonics in the inner Northern Apennines (Siena Basin, southern Tuscany, Italy) and their seismotectonic implication. Journal of Geodynamics 76, 25–45.
Brogi, A., Alçiçek, M.C., Yalçıner, C.Ç., Capezzuoli, E., Liotta, D., Meccheri, M., Rimondi, V., Ruggieri, G., Gandin, A., Boschi, C., Büyüksaraç, A., Alçiçek, H., Bülbül, A., Baykara, M.O., Shen, C.-C., 2016. Hydrothermal fluids circulation and travertine deposition in an active tectonic setting: insights from the Kamara geothermal area (western Anatolia, Turkey). Tectonophysics 680, 211–232.
Cai, Y., Cheng, H., An, Z., Edwards, R.L., Wang, X., Tan, L., Wang, J., 2010. Large variations of oxygen isotopes in precipitation over south-central Tibet during marine isotope stage 5. Geology 38 (3), 243–246.
Cai, Y.J., Fung, I.Y., Edwards, R.L., An, Z.S., Cheng, H., Lee, J.E., Tan, L.C., Sheng, C.C., Wang, X.F., Day, J.A., Zhou, W.J., Kelly, M.J., Chiang, J.C.H., 2015. Variability of stalagmite-inferred Indian monsoon precipitation over the past 252,000 y. Proceedings of the National Academy of Sciences of the United States of America 112 (10), 2954–2959.
Capezzuoli, E., Gandin, A., Pedley, M., 2014. Decoding tufa and travertine (fresh water carbonates) in the sedimentary record: the state of the art. Sedimentology 61 (1), 1–21.
Chafetz, H.S., Folk, R.L., 1984. Travertines — depositional morphology and the bacterially constructed constituents. Journal of Sedimentary Petrology 54 (1), 289–316.
Chafetz, H.S., Guidry, S.A., 1999. Bacterial shrubs, crystal shrubs, and ray-crystal shrubs: bacterial vs. abiotic precipitation. Sedimentary Geology 126 (1–4), 57–74.
Chen, Q.Z., Freymueller, J.T., Yang, Z.Q., Xu, C.J., Jiang, W.P., Wang, Q., Liu, J.N., 2004. Spatially variable extension in southern Tibet based on GPS measurements. Journal of Geophysical Research-Solid Earth 109 (B9). http://dx.doi.org/10.1029/2002JB002350.
Cheng, H., Edwards, R.L., Hoff, J., Gallup, C.D., Richards, D.A., Asmerom, Y., 2000. The half-lives of uranium-234 and thorium-230. Chemical Geology 169 (1–2), 17–33.
Claes, H., Soete, J., Van Noten, K., El Desouky, H., Marques Erthal, M., Vanhaecke, F., Özkul, M., Swennen, R., 2015. Sedimentology, three-dimensional geobody reconstruction and carbon dioxide origin of Pleistocene travertine deposits in the Ballik area (south-west Turkey). Sedimentology 62 (5), 1408–1445.
Croci, A., Della Porta, G., Capezzuoli, E., 2016. Depositional architecture of a mixed travertine-terrigenous system in a fault-controlled continental extensional basin (Messinian, Southern Tuscany, Central Italy). Sedimentary Geology 332, 13–39.
Damm, B., Felderer, A., 2013. Impact of atmospheric warming on permafrost degradation and debris flow initiation — a case study from the eastern European Alps. E&G Quaternary Science Journal 62 (2), 136–149.
De Filippis, L., Faccenna, C., Billi, A., Anzalone, E., Brilli, M., Soligo, M., Tuccimei, P., 2013. Plateau versus fissure ridge travertines from Quaternary geothermal springs of Italy and Turkey: interactions and feedbacks between fluid discharge, paleoclimate, and tectonics. Earth-Science Reviews 123, 35–52.
Della Porta, G., 2015. Carbonate Build-Ups in Lacustrine, Hydrothermal and Fluvial Settings: Comparing Depositional Geometry, Fabric Types and Geochemical Signature. Microbial Carbonates in Space and Time: Implications for Global Exploration and Production 418 pp. 17–68.
Dupraz, C., Reid, R.P., Braissant, O., Decho, A.W., Norman, R.S., Visscher, P.T., 2009. Processes of carbonate precipitation in modern microbial mats. Earth-Science Reviews 96 (3), 141–162.
Eyles, N., Eyles, C.H., Miall, A.D., 1983. Lithofacies types and vertical profile models: an alternative approach to the description and environmental interpretation of glacial diamict and diamictite sequences. Sedimentology 30, 393–410.
Faccenna, C., Soligo, M., Billi, A., De Filippis, L., Funiciello, R., Rossetti, C., Tuccimei, P., 2008. Late Pleistocene depositional cycles of the Lapis Tiburtinus travertine (Tivoli, Central Italy): possible influence of climate and fault activity. Global and Planetary Change 63 (4), 299–308.
Folk, R.L., 1994. Interaction between bacteria, nanobacteria, and mineral precipitation in hot-springs of central Italy. Geographie Physique et Quaternaire 48 (3), 233–246.
Fouke, B.W., 2011. Hot-spring systems geobiology: abiotic and biotic influences on travertine formation at Mammoth Hot Springs, Yellowstone National Park, USA. Sedimentology 58 (1), 170–219.
Fouke, B.W., Farmer, J.D., Des Marais, D.J., Pratt, L., Sturchio, N.C., Burns, P.C., Discipulo, M.K., 2000. Depositional facies and aqueous-solid geochemistry of travertine depositing hot springs (Angel Terrace, Mammoth Hot Springs, Yellowstone National Park, USA). Journal of Sedimentary Research 70, 265–285.
Frank, N., Braum, M., Hambach, U., Mangini, A., Wagner, G., 2000. Warm period growth of travertine during the last interglaciation in southern Germany. Quaternary Research 54 (1), 38–48.
French, H.M., 2007. The Periglacial Environment. John Wiley & Sons Ltd, Chichester, UK.
Frisia, S., Borsato, A., Karst, 2010. Carbonates in Continental Settings: Geochemistry, Diagenesis and Applications. In: Alonso-Zarza, A.M., Tanner, L.H. (Eds.), Elsevier, Amsterdam, pp. 179–214.
Gandin, A., Capezzuoli, E., 2014. Travertine: distinctive depositional fabrics of carbonates from thermal spring systems. Sedimentology 61, 264–290.
Gao, J., Zhou, X., Fang, B., Li, T., Tang, L., 2013. U-series dating of the travertine depositing near the Rongma Hot Springs in northern Tibet, China, and its paleoclimatic implication. Quaternary International 298, 98–106.
Garnett, E.R., Gilmour, M.A., Rowe, P.J., Andrews, J.E., Preece, R.C., 2004. ^{230}Th/^{234}U dating of Holocene tufas: possibilities and problems. Quaternary Science Reviews 23 (7–8), 947–958.
Ge, S., Wu, Q.B., Lu, N., Jiang, G.L., Ball, L., 2008. Groundwater in the Tibet Plateau, western China. Geophysical Research Letters 35 (18). http://dx.doi.org/10.1029/2008GL034809.
Gradziński, M., Wróblewski, W., Duliński, M., Hercman, H., 2014. Earthquake-affected development of a travertine ridge. Sedimentology 61 (1), 238–263.
Grün, R., Schwarcz, H.P., Ford, D.C., Hentzsch, B., 1988. ESR dating of spring deposited travertines. Quaternary Science Reviews 7, 429–432.
Guo, L., Riding, R., 1992. Aragonite laminae in hot water travertine crusts, Rapolano-Terme, Italy. Sedimentology 39 (6), 1067–1079.
Guo, L., Riding, R., 1998. Hot-spring travertine facies and sequences, Late Pleistocene, Rapolano Terme, Italy. Sedimentology 45 (1), 163–180.
Han, T., 1981. Relationship of the Active Structural System to Geothermal Activity in Southern Xizang (Tibet), in Himalayan Geology II. Geological Press, Beijing, pp. 45–58 (in Chinese).
Hancock, P.L., Chalmers, R.M.L., Altunel, E., Cakir, Z., 1999. Travitonics: using travertines in active fault studies. Journal of Structural Geology 21 (8), 903–916.
Heimann, A., Sass, E., 1989. Travertines in the northern Hula Valley, Israel. Sedimentology 36 (1), 95–108.
Hill, C.L., 2001. Geological contexts of the Acheulian (Middle Pleistocene) in the Eastern Sahara. Geoarchaeology 16, 65–94.
Hoffmann, D.L., 2008. ^{230}Th isotope measurements of femtogram quantities for U-series dating using multi ion counting (MIC) MC-ICPMS. International Journal of Mass Spectrometry 275 (1–3), 75–79.

Hoffmann, D.L., Prytulak, J., Richards, D.A., Elliott, T., Coath, C.D., Smart, P.L., Scholz, D., 2007. Procedures for accurate U and Th isotope measurements by high precision MC-ICPMS. International Journal of Mass Spectrometry 264 (2–3), 97–109.
Holden, N.E., 1990. Total half-lives for selected nuclides. Pure and Applied Chemistry 62 (5), 941–958.
Jaffey, A.H., Flynn, K.F., Glendenin, L.E., Bentley, W.C., Essling, A.M., 1971. Precision measurement of half-lives and specific activities of ^{235}U and ^{238}U. Physical Review C 4 (5), 1889–1906.
Jones, B., Renaut, R.W., 1995. Noncrystallographic calcite dendrites from hot spring deposits in Kenya. Journal of Sedimentary Research 65, 154–169.
Jones, B., Renaut, R.W., 2008. Cyclic development of large, complex, calcite dendrite crystals in the Clinton travertine, Interior British Columbia, Canada. Sedimentary Geology 203 (1–2), 17–35.
Jones, B., Renaut, R.W., 2010. Calcareous spring deposits in continental settings. In: Alonso-Zarza, A.M., Tanner, L.H. (Eds.), Carbonates in Continental Settings: Geochemistry, Diagenesis and Applications. Elsevier, Amsterdam, pp. 179–214.
Jones, B., Renaut, R.W., Rosen, M.R., 2000. Trigonal dendritic calcite crystals forming from hot spring waters at Waikite, North Island, New Zealand. Journal of Sedimentary Research 70, 586–603.
Jones, B., Renaut, R.W., Owen, R.B., Torfason, H., 2005. Growth patterns and implications of complex dendrites in calcite travertines from Lýsuhóll, Snæfellsnes, Iceland. Sedimentology 52 (6), 1277–1301.
Kaiser, K., Schoch, W.H., Miehe, G., 2007. Holocene paleosols and colluvial sediments in Northeast Tibet (Qinghai Province, China): properties, dating and paleoenvironmental implications. Catena 69 (2), 91–102.
Kaiser, K., Opgenoorth, L., Schoch, W.H., Miehe, G., 2009. Charcoal and fossil wood from palaeosols, sediments and artificial structures indicating Late Holocene woodland decline in southern Tibet (China). Quaternary Science Reviews 28 (15–16), 1539–1554.
Kathayat, G., Cheng, H., Sinha, A., Spotl, C., Edwards, R.L., Zhang, H.W., Li, X.L., Yi, L., Ning, Y.F., Cai, Y.J., Lui, W.G.L., Breitenbach, S.F.M., 2016. Indian monsoon variability on millennial–orbital timescales. Scientific Reports 6, 24374. http://dx.doi.org/10.1038/srep24374.
Kitano, Y., 1963. Geochemistry of calcareous deposits found in hot springs. Journal of Science, Nagoya University 11, 68–100.
Liu, Z.H., Sun, H.L., Lu, B.Y., Liu, X.L., Ye, W.B., Zeng, C., 2010. Wet-dry seasonal variations of hydrochemistry and carbonate precipitation rates in a travertine-depositing canal at Baishuitai, Yunnan, SW China: implications for the formation of biannual laminae in travertine and for climatic reconstruction. Chemical Geology 273 (3–4), 258–266.
Love, K.M., Chafetz, H.S., 1988. Diagenesis of laminated travertine crusts, Arbuckle Mountains, Oklahoma. Journal of Sedimentary Petrology 58 (3), 441–445.
Mahan, S.A., Miller, D.M., Menges, C.M., Yount, J.C., 2007. Late Quaternary stratigraphy and luminescence geochronology of the northeastern Mojave Desert. Quaternary International 166, 61–78.
Mallick, R., Frank, N., 2002. A new technique for precise uranium-series dating of travertine micro-samples. Geochimica et Cosmochimica Acta 66 (24), 4261–4272.
McGarry, S.F., Baker, A., 2000. Organic acid fluorescence: applications to speleothem palaeoenvironmental reconstruction. Quaternary Science Reviews 19 (11), 1087–1101.
Minissale, A., Kerrick, D.M., Magro, G., Murrell, M.T., Paladini, M., Rihs, S., Sturchio, N.C., Tassi, F., Vaselli, O., 2002. Geochemistry of Quaternary travertines in the region north of Rome (Italy): structural, hydrologic and paleoclimatic implications. Earth and Planetary Science Letters 203 (2), 709–728.
Nemec, W., Kazanci, N., 1999. Quaternary colluvium in west-central Anatolia: sedimentary facies and palaeoclimatic significance. Sedimentology 46, 139–170.
Özkul, M., Varol, B., Alçiçek, M.C., 2002. Depositional environments and petrography of Denizli travertines. Bulletin of the Mineral Research and Exploration 125, 13–29.
Özkul, M., Gokgoz, A., Kele, S., Baykara, M.O., Shen, C.C., Chang, Y.W., Kaya, A., Hancer, M., Aratman, C., Akin, T., Özkul, Z., 2014. Sedimentological and geochemical characteristics of a fluvial travertine: a case from the eastern Mediterranean region. Sedimentology 61 (1), 291–318.
Parkhurst, D.L., Appelo, C.A.J., 2013. Description of Input and Examples for PHREEQC Version 3—A Computer Program for Speciation, Batch-Reaction, One-Dimensional Transport, and Inverse Geochemical Calculations. U.S. Geological Survey Techniques and Methods, Book 6 (chap. A43, 497 pp., available only at http://pubs.usgs.gov/tm/06/a43/).
Pedley, M., 1992. Fresh-water (phytoherm) reefs — the role of biofilms and their bearing on marine reef cementation. Sedimentary Geology 79 (1–4), 255–274.
Pellicer, X.M., Linares, R., Gutiérrez, F., Comas, X., Roqué, C., Carbonel, D., Zarroca, M., Rodríguez, J.A.P., 2014. Morpho-stratigraphic characterization of a tufa mound complex in the Spanish Pyrenees using ground penetrating radar and trenching, implications for studies in Mars. Earth and Planetary Science Letters 388, 197–210.
Pentecost, A., 1995. The Quaternary travertine deposits of Europe and Asia Minor. Quaternary Science Reviews 14, 1005–1028.
Pentecost, A., 2005. Travertine. Springer, Berlin (445 pp.).
Pola, M., Gandin, A., Tuccimei, P., Soligo, M., Deiana, R., Fabbri, P., Zampieri, D., 2014. A multidisciplinary approach to understanding carbonate deposition under tectonically controlled hydrothermal circulation: a case study from a recent travertine mound in the Euganean hydrothermal system, northern Italy. Sedimentology 61, 172–199.
Public Weather Service Center of China. Lhasa Climate Normals, 1971–2000a. http://www.weather.com.cn/html/cityintro/101140101.shtml.
Rainey, D.K., Jones, B., 2009. Abiotic versus biotic controls on the development of the Fairmont Hot Springs carbonate deposit, British Columbia, Canada. Sedimentology 56 (6), 1832–1857.
Rennert, T., Händel, M., Höschen, C., Lugmeier, J., Steffen, M., Totsche, K.U., 2014. A NanoSIMS study on the distribution of soil organic matter, iron and manganese in a nodule from a Stagnosol. European Journal of Soil Science 65, 684–692.
Rich, J., Stokes, S., Wood, W., Bailey, R., 2003. Optical dating of tufa via in situ aeolian sand grains: a case example from the Southern High Plains, USA. Quaternary Science Reviews 22 (10–13), 1145–1152.
Sanders, D.G., Ostermann, M., Kramers, J., 2010. Meteoric diagenesis of Quaternary carbonate-rocky talus slope successions (Northern Calcareous Alps, Austria). Facies 56 (1), 27–46.
Schulte, L., Julia, R., Burjachs, F., Hilgers, A., 2008. Middle Pleistocene to Holocene geochronology of the River Aguas terrace sequence (Iberian Peninsula): fluvial response to Mediterranean environmental change. Geomorphology 98 (1–2), 13–33.
Smith, J.R., Giegengack, R., Schwarcz, H.P., 2004. Constraints on Pleistocene pluvial climates through stable-isotope analysis of fossil-spring tufas and associated gastropods, Kharga Oasis, Egypt. Paleogeography, Paleoclimatology, Paleoecology 206, 157–175.
Smith, J.R., Hawkins, A.L., Asmerom, Y., Polyak, V., Giegengack, R., 2007. New age constraints on the Middle Stone Age occupations of Kharga Oasis, Western Desert, Egypt. Journal of Human Evolution 52, 690–701.
Stone, A.E.C., Viles, H.A., Thomas, L., Van Calsteren, P., 2010. Can ^{234}U–^{230}Th dating be used to date large semi-arid tufas? Challenges from a study in the Naukluft Mountains, Namibia. Journal of Quaternary Science 25 (8), 1360–1372.
Stoops, G., 2003. Guidelines for Analysis and Description of Soil and Regolith Thin Section. Soil Science Society of America, Inc. Madison, Wisconsin, USA.
Takashima, C., Kano, A., 2008. Microbial processes forming daily lamination in a stromatolitic travertine. Sedimentary Geology 208 (3–4), 114–119.
Tan, H.B., Zhang, Y.F., Zhang, W.J., Kong, N., Zhang, Q., Huang, J.Z., 2014. Understanding the circulation of geothermal waters in the Tibetan Plateau using oxygen and hydrogen stable isotopes. Applied Geochemistry 51, 23–32.
Taylor, M., Yin, A., Ryerson, F.J., Kapp, P., Ding, L., 2003. Conjugate strike-slip faulting along the Bangong-Nujiang suture zone accommodates coeval east–west extension and north–south shortening in the interior of the Tibetan Plateau. Tectonics 22 (4). http://dx.doi.org/10.1029/2002TC001361.
Tian, L.D., Yao, T.D., Numaguti, A., Sun, W.Z., 2001. Stable isotope variations in monsoon precipitation on the Tibetan Plateau. Journal of the Meteorological Society of Japan 79 (5), 959–966.
Toker, E., Kayseri-Özer, M.S., Özkul, M., Kele, S., 2015. Depositional system and palaeoclimatic interpretations of Middle to Late Pleistocene travertines: Kocabaş, Denizli, south-west Turkey. Sedimentology 62 (5), 1360–1383.
Tong, W., Liao, Z., Liu, S., Zhang, Z., You, M., Zhang, M., 2000. Thermal Springs in Tibet. Science Press, Beijing (in Chinese).
Vazquez-Urbez, M., Pardo, G., Arenas, C., Sancho, C., 2011. Fluvial diffluence episodes reflected in the Pleistocene tufa deposits of the River Piedra (Iberian Range, NE Spain). Geomorphology 125 (1), 1–10.
Viles, H., Pentecost, A., 2007. Tufa and travertine. In: Nash, D., McLaren, S. (Eds.), Geochemical Sediments and Landscapes. Blackwell, Oxford, pp. 173–199.
Wang, B.L., French, H.M., 1995. Permafrost on the Tibet Plateau, China. Quaternary Science Reviews 14, 255–274.
Wedepohl, K.H., 1995. The composition of the continental-crust. Geochimica et Cosmochimica Acta 59 (7), 1217–1232.
Xie, Y.W., Liu, H.F., Qiangba, Z.X., Jiang, G.W., 2010. Determination of the formation sequence of Chaqupu Formation of Early-Middle Triassic in the Quesang area, Tibet. Geological Bulletin of China 29 (12), 1833–1839 (in Chinese with English abstract).
Yin, A., Harrison, T.M., 2000. Geologic evolution of the Himalayan–Tibetan orogen. Annual Review of Earth and Planetary Sciences 28, 211–280.
Zentmyer, R., Myrow, P.M., Newell, D.L., 2008. Travertine deposits from along the South Tibetan Fault System near Nyalam, Tibet. Geological Magazine 145 (6), 753–765.
Zhang, D.D., 1997. An interpretation of some observations on karst spring regimes and their implication for underground drainage systems in Lhasa karst area, Tibet. Asian Geographer 16, 59–71.
Zhang, D.D., Li, S.H., 2002. Optical dating of Tibetan human hand- and footprints: an implication for the palaeoenvironment of the last glaciation of the Tibetan Plateau. Geophysical Research Letters 29 (5), 1072–1074.
Zhang, D.D., Li, S.H., He, Y.Q., Li, B.S., 2003. Human settlement of the last glaciation on the Tibetan Plateau. Current Science 84 (5), 701–704.
Zhao, Y.Y., Zhao, X.T., Ma, Z.B., 2006. Study on chronology for hot spring typed Cs-deposit of Targjia, Tibet. Acta Petrologica Sinica 22 (3), 717–724.
Zhao, Y.Y., Cui, Y.B., Zhao, X.T., 2010. Geological and geochemical features and significance of travertine in travertine-island from Zhabuye salt lake, Tibet, China. Geological Bulletin of China 29 (1), 124–141.
Zhu, L.P., Lu, X.M., Wang, J.B., Peng, P., Kasper, T., Daut, G., Haberzettl, T., Frenzel, P., Li, Q., Yang, R.M., Schwalb, A., Mausbacher, R., 2015. Climate change on the Tibetan Plateau in response to shifting atmospheric circulation since the LGM. Scientific Reports 5, 13318. http://dx.doi.org/10.1038/srep13318.